JOURNAL OF GEOPHYSICAL RESEARCH, VOL. 115, C03003, doi:10.1029/2009JC005300, 2010



# An altimetry-based gravest empirical mode south of Africa: 2. Dynamic nature of the Antarctic Circumpolar Current fronts

Sebastiaan Swart[1] and Sabrina Speich[2]

Received 23 January 2009; revised 31 August 2009; accepted 22 September 2009; published 2 March 2010.

[1] Swart et al. (2010) applied altimetry data to the gravest empirical mode south of Africa to yield a 16 year time series of temperature and salinity sections. In this study we use these thermohaline sections to derive weekly estimates of heat content (HC) and salt content (SC) at the GoodHope meridional transect of the Antarctic Circumpolar Current (ACC). These estimates compare favorably to observed data. The resulting 16 year time series of HC and SC estimates are used to explain the subsurface thermohaline variability at each ACC front and frontal zone. The variability at the Subantarctic Zone (SAZ) is principally driven by the presence of Agulhas Rings, which occur in this region approximately 2.7 times per annum and are responsible for the longest and highest scales of observed variability. The variability of the SAZ is responsible for over 50% and 60% of the total ACC HC and SC variability, respectively. Poleward of the SAZ, the variability is largely determined by the influence of the local topography on the fronts of the region and can be explained by the conservation of potential vorticity. Wavelet analysis is conducted on the time series of meridionally integrated HC and SC in each ACC front and frontal zone, revealing a consistent seasonal mode that becomes more dominant toward the southern limit of the ACC. The lower-frequency signals are compared with two dominant modes of variability in the Southern Ocean. The Southern Annular Mode correlates well with the HC and SC anomaly estimates at the Antarctic Polar Front, while the Southern Oscillation Index appears to have connections to the variability found in the very southern domains of the ACC.

**Citation:** Swart, S., and S. Speich (2010), An altimetry-based gravest empirical mode south of Africa: 2. Dynamic nature of the Antarctic Circumpolar Current fronts, *J. Geophys. Res.*, *115*, C03003, doi:10.1029/2009JC005300.

## 1. Introduction

[2] The Antarctic Circumpolar Current (ACC) consists of multiple branches and filaments that are grouped together to represent the main ACC fronts [*Sokolov and Rintoul*, 2007a, 2007b, 2009a, 2009b; *Swart et al.*, 2008]. The fronts often exhibit considerable latitudinal variability on their circumpolar path, as was first noticed by *Deacon* [1933] over 70 years ago. These forms of variability are dominant in the mesoscale band induced by front meandering and eddy genesis [*Mackintosh*, 1946; *Joyce et al.*, 1978; *Lutjeharms and Valentine*, 1988; *Stammer*, 1998; *Moore et al.*, 1999; *Phillips and Rintoul*, 2000; *Morrow et al.*, 2004] and are vital to meridional fluxes of heat and salt within the Southern Ocean. This suggests that a large portion of the variability of the ACC is determined by the individual behavior of the ACC fronts and, to a lesser degree, the regions between the fronts. To date, little work has been done to better understand the fronts' regional and temporal variability, notably in the African sector of the Southern Ocean [*Koshlyakov et al.*, 1985; *Nowlin and Klinck*, 1986; *Gouretski and Danilov*, 1994; *Ansorge et al.*, 2006].

[3] Previous measurements of heat content (HC) and salt content (SC) in the Southern Ocean have been based on few synoptic hydrographic transects, the majority of which were completed in austral summer only. To overcome the poor temporal and spatial resolution of measurements in the African sector of the Southern Ocean, we make use of the gravest empirical mode (GEM) method, first described for the Southern Ocean by *Sun and Watts* [2001], and apply this technique to weekly composites of satellite altimetry data. The GEM method makes use of all available hydrographic casts from the southeastern sector of the Atlantic Ocean and projects the data into a baroclinic stream function space, parameterized by pressure and dynamic height. Further details can be found in section 2.2. The development and validation of this method is described in Part 1 of this study [*Swart et al.*, 2010, hereafter Part 1]. From the GEM, we derive the subsurface HC and SC structure, along a permanent geographic locale, enabling us to better understand the temporal variability associated with the region and the ACC system. The GoodHope (GH) line is the geographic locale used in this study [*Ansorge et al.*, 2004; *Speich and Arhan*, 2007]. The GH program provides the ideal platform to

[1]Department of Oceanography, University of Cape Town, Rondebosch, South Africa.
[2]Laboratoire de Physique des Océans, UMR 6523, Université de Bretagne Occidentale, CNRS, IFREMER, Brest, France.


0148-0227/10/2009JC005300$09.00

combine the GEM with satellite altimetry, as demonstrated by Part 1.

[4] The GH line crosses the southeast Atlantic Ocean, which is recognized one of the most dynamic and variable ocean domains in the world [*Wunsch and Stammer*, 1995; *Boebel et al.*, 2003]. This region is identified as the meeting point of the eastward flowing ACC and the Agulhas Current, acknowledged as one of the world's strongest western boundary currents [*Bryden et al.*, 2005; *Lutjeharms*, 2006]. The Agulhas Current's westward termination is marked by the Agulhas Retroflection, which produces an intermittent stream of Agulhas Rings [*Gordon*, 1985; *Lutjeharms and Gordon*, 1987; *Duncombe-Rae*, 1991; *Lutjeharms*, 1996; *de Ruijter et al.*, 1999; *Boebel et al.*, 2003; *Lutjeharms*, 2006] that generally propagate in a northwesterly direction [*Schonten et al.*, 2000]. Irregularly Agulhas Rings propagate on a west to southwest course. These features directly influence the stability and continuity of the Subtropical Front (STF) [*Lutjeharms*, 1988; *Lutjeharms and Valentine*, 1988; *Belkin and Gordon*, 1996; G. Dencausse et al., Routes of Agulhas rings in the southeastern Cape Basin, submitted to *Deep Sea Research Part I*, 2009] and have been located and sampled in the Subantarctic Zone (SAZ) [*Swart et al.*, 2008; *Gladyshev et al.*, 2008]. These anomalies may play a significant role in the local variability of the northern ACC region, which has implications for the behavior of local biology and biogeochemistry.

[5] The GEM-produced sections of temperature and salinity are used in this study to quantify the property signatures of these features and the possible impact they may have in the region. We also evaluate the role elevated topography and bathymetric passages may have in bringing about instabilities to the flow of the ACC fronts, at the GH line. The final parts of this study make use of meridionally integrated GEM estimates of HC and SC to quantify the variability experienced in the region. An attempt to connect the long-term variability with the well-known modes of Southern Hemisphere atmospheric variability is also briefly covered.

## 2. Material and Methods

### 2.1. Data

[6] Data from eight conductivity-temperature-depth (CTD) sections, conducted between 1984 and 2005, are used to set up the GEM fields for the oceanic region connecting the southwestern tip of South Africa and the Antarctic continent via the Greenwich Meridian (see Part 1). Included are two repeat high-resolution (average station spacing is 50 km) CTD sections along the GH line [*Gladyshev et al.*, 2008; *Swart et al.*, 2008]. The "Maps of Sea Level Anomaly" (MSLA) and "Maps of Absolute Dynamic Topography" (MADT) data, available from CLS/AVISO have been used in this study. Both products are constructed on a 1/3° Mercator grid and are available between 14 October 1992 and 23 January 2008, at weekly intervals. This yields a continuous time series of 798 weeks of data. We choose to use the "up-to-date" data files that make use of all the altimeter data available for each period because it is best suited at resolving the fine-scale structures and variability associated with the ACC.

### 2.2. GEM

[7] Hydrographic casts of temperature and salinity are projected into stream function space, parameterized by pressure and dynamic height. This method demonstrates the remarkable relationship between the surface dynamic height (relative to 2500 dbar) and the subsurface thermohaline structure, which has been tested across the ACC south of Africa by Part 1. Parameterizing hydrographic data in this way captures more than 97% of the temperature and density variance and 93% of the salinity variance between the surface and 2500 dbar (Part 1).

[8] The GEM fields retain many of the characteristic hydrographic features normally identified when observed data are represented in geographic space. To emphasize this, a comparison between the vertical profile of the hydrographic variables and the GEM fields is shown in Figure 1. Each set of vertical temperature and salinity profiles (thin curves) are representative of a dynamic height cluster that has a range of 0.01 dynamic (dyn) m (1 dyn m = 10 $m^2$ $s^{-2}$). The gray curve represents the mean GEM vertical structure within the same dynamic height range as those of the observed temperature and salinity profiles. The consistency between the two representations emphasizes the ability to parameterize thermohaline variables by dynamic height in this region. Examples of these include the subsurface temperature minimum layer in the upper 200 dbar, located south of the Antarctic Polar Front (APF) and the characteristically low saline waters, associated with the Antarctic Intermediate Water layer, extending between the surface and approximately 1000 dbar. The variation in the depth of the thermocline between the five grouping has a large effect on the similarity of the vertical structures between the two representations. The profiles, for example, within the 1.9 dyn m grouping, exhibit less defined vertical structure in the upper 600 dbar, due to a deeper thermocline, while the profiles, within the 0.7 dyn m grouping, display very similar structure below 200 dbar, due to a shallower thermocline. The GEM reveals its efficiency at removing the small-scale variations in the vertical structure that are represented as the small fluctuations in the real data.

[9] Parameterizing the data by pressure and dynamic height allows us to apply this method to altimeter-derived absolute dynamic height (ADT) data. This yields a continuous time series of temperature and salinity profiles, across the ACC (1992–2008), and forms the basis for the analysis in this study. The ADT is produced by combining altimeter Sea Surface Height (SSH) anomalies to a mean dynamic height state, derived from repeat hydrographic sections (CTD and XBT), at the GH line [*Swart et al.*, 2008]. The ADT is combined with the GEM to create the altimetry GEM (AGEM). For further details on the construction of the ADT and the AGEM, refer to *Swart et al.* [2008] and Part 1, respectively.

### 2.3. Front Positions

[10] Altimetry SSH data has proven to be largely representative of the baroclinic shear in the water column. This indicates that local maxima in the dynamic height gradient are representative of the maximum baroclinic shear, associated with fronts [*Hughes and Ash*, 2001; *Sokolov and Rintoul*, 2007a, 2007b, 2009a, 2009b; *Swart et al.*, 2008]. In

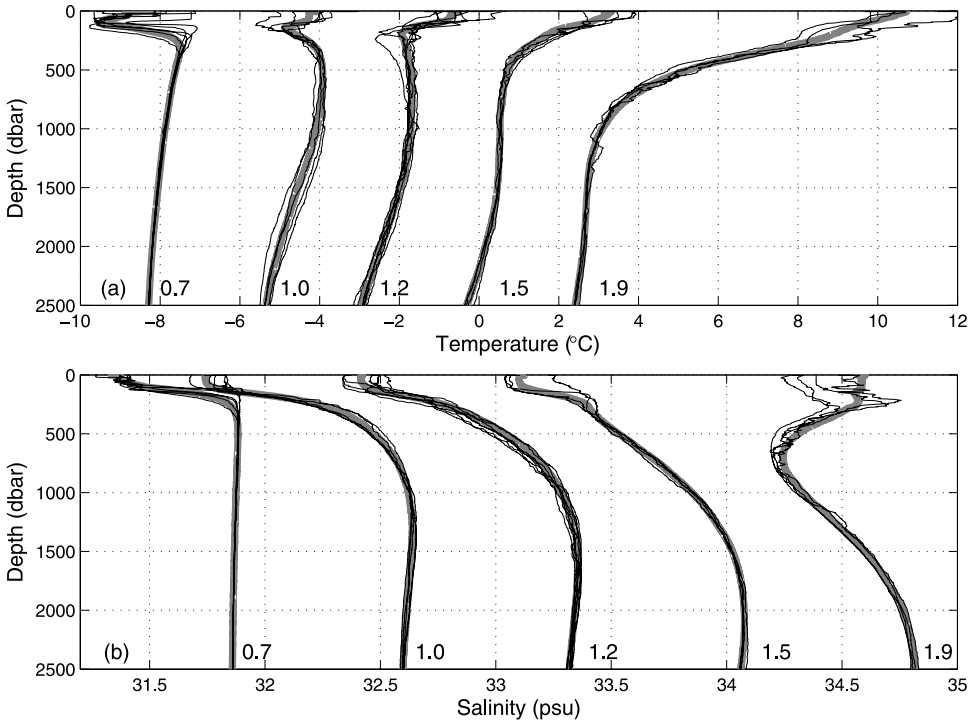


**Figure 1.** Groupings of observed (a) temperature and (b) salinity profiles (thin black curves) that are found within 0.01 dyn m of the central values displayed. The thick gray curves show the corresponding GEM-estimated profiles. The temperature profiles are each offset to the left by 2°C and the salinity profiles are each offset to the left by 0.7 psu.

this study we make use of both the core positions of the ACC fronts, and the frontal boundary zones (region between two limits that consistently capture the maximum frontal velocities). These boundaries are located by exploiting both the height and geostrophic velocity information from the MADT data, at the GH line. A complete description of the methodology used to define the core position of the ACC fronts can be found in Part 1 (section 5.2). The methodology used to define the frontal boundary zones has been described by *Swart et al.* [2008]. In brief, these limits are defined as follows: continuous isolines of MADT data follow the lowest velocity magnitudes in between the main fronts throughout the altimetry time series. These MADT isolines, therefore, depict the boundary between successive fronts. This allows us to define the spatial volume of each individual front, thus providing a more accurate measurement of the HC and SC related to that particular front. Table 1 outlines all frontal zones discussed in this study, including their abbreviations, latitudinal ranges and mean widths.

### 2.4. Heat and Salt Content

[11] The HC and SC is integrated throughout the upper 2500 dbar of the water column. The HC is calculated in the conventional manner

$$HC = \int_0^{2500} \rho C_p T dz, \tag{1}$$

where $\rho$ is the density of seawater (1027 kg $m^{-3}$), $Cp$ is the heat capacity of seawater at constant pressure (4000 J $kg^{-1}$ $K^{-1}$), $dz$ is the thickness of the water column, and $T$ is the potential temperature (in °C). The SC is estimated as follows:

$$SC = \int_0^{2500} 0.001 \rho S dz, \tag{2}$$

where $S$ is the salinity.

## 3. Comparing the GEM-Derived Heat and Salt Content With Direct Observations

[12] The ability of the AGEM to accurately capture the thermohaline structure of the ACC south of Africa has been demonstrated in the first part of this study (Part 1). To further validate the results presented in this paper, we compare the HC and SC, deduced from temperature and salinity sections produced by the AGEM, to in situ observations from repeat CTD occupations at the GH line

**Table 1.** Abbreviations, Latitudinal Ranges, and Mean Widths of the Frontal Zones Described in This Study

| Frontal Zone | Abbreviation | Latitudinal Range (°S) | Mean Width (km) |
|---|---|---|---|
| Subantarctic Zone | SAZ | 38.2–46.8 | 540 |
| Antarctic Polar Frontal Zone | APZ | 43.7–51.2 | 573 |
| Southern ACC Zone | SACCZ | 47.6–54.9 | 440 |
| Southern Boundary Zone | SBZ | 51.8–57.8 | 217 |

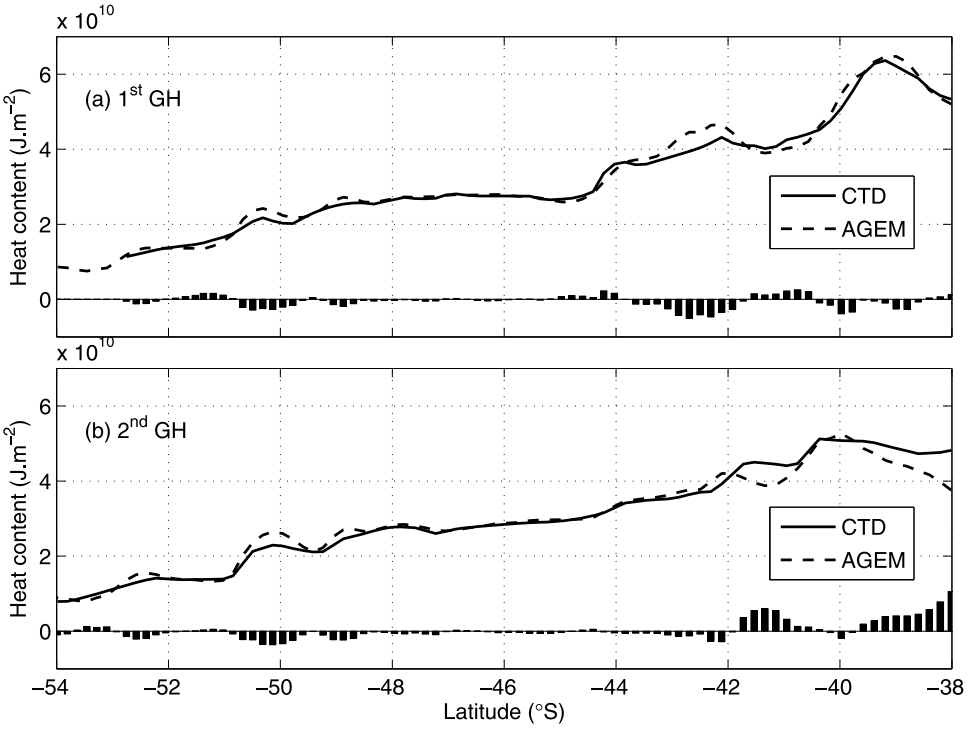


**Figure 2.** Comparison between observed (solid curve) and AGEM-estimated (dashed curve) heat content between the surface and 2500 dbar for the (a) first and (b) second GH occupations, completed in November 2004 and October 2005, respectively. The difference between the hydrographic and AGEM estimates (bars) are displayed along the *x* axis.

(Figures 2 and 3). Prior to calculating the HC and SC, using the AGEM, the GEM fields are recalculated, after excluding the observed section to which it is being compared to. This is to ensure that the reproduced data are fully independent of the directly measured data.

[13] The HC and SC meridional gradients in the observed and AGEM-produced data sets compare well. The representations are particularly similar at the Antarctic Polar Frontal Zone (APZ; between 44 and 49°S) where HC gains and mesoscale perturbations are especially weak (to be illustrated in section 4). Elevated differences (shown along the *x* axis in Figures 2 and 3c) are located over the APF at approximately 50°S. This may be explained by the higher-mesoscale variability found at this front (explained in more detail in section 4). Within the ACC domain, the highest differences are found in the Subantarctic Zone (roughly between 40 and 45°S). The intrusion of subtropical waters by eddy features and strong meanders at the STF, and on occasions Agulhas Waters [*Swart et al.*, 2008; *Gladyshev et al.*, 2008] by Agulhas Rings, reduce the accuracy of the GEM in this region. This is because the GEM relies on the principle that temperature and salinity values be aligned with a single value of dynamic height [*Sun and Watts*, 2001]. The large discrepancy of >200 kg $m^{-2}$ in SC at ~41°S, for the second CTD occupation, is caused by the inability of the AGEM to accurately capture the salinity magnitude associated with an Agulhas Ring that was crossed during the CTD transect (see *Swart et al.* [2008] and Part 1 for further details on the hydrographic and altimetric structure of this particular feature). North of ~40°S and extraneous to the ACC, the GEM's accuracy to determine the observed thermohaline structure decreases sharply with concomitant increases in errors. This is due to the high level of mixing of very different water masses associated with the known mesoscale turbulence and Indo-Atlantic exchange taking place in this region [*Duncombe-Rae*, 1991; *Lutjeharms*, 1996; *de Ruijter et al.*, 1999; *Boebel et al.*, 2003]. The consequence of this is that the relationship between temperature and salinity and the dynamic height changes and is no longer one to one. The root-mean-square (RMS) error in HC and SC, due to the presence of Agulhas Rings between 38 and 42°S, is estimated as $4.22 \times 10^9 \pm 0.14 \times 10^9$ J $m^{-2}$ and $170.6 \pm 24$ kg $m^{-2}$, respectively.

[14] Eddy variations in the HC and SC are captured by the AGEM, yet these variations are somewhat exaggerated (refer to section 5.5 of Part 1 for a more detailed description of AGEM exaggeration of mesoscale features). A portion of the differences could be explained by errors introduced to the altimeter data used to create the ADT time series [*Le Traon et al.*, 1998]. Further discrepancies could, in part, come from the SSH signal that includes a barotropic component, which we are yet unable to isolate in in situ observations due to a lack of information about the Earth's geoid [*Swart et al.*, 2008]. Last, differences in spatial and temporal sampling between the altimeter and in situ observations may introduce additional errors. The mean RMS differences between the observed and AGEM-estimated HC and SC, between the surface and 2500 dbar, are $1.22 \times 10^9$ J $m^{-2}$ and 39.8 kg $m^{-2}$, respectively. Major differences are associated with the upper layers, where variability at all scales is the largest. Nonetheless, the RMS represents less than 10% of the signal. We can therefore trust the method and reconstruct

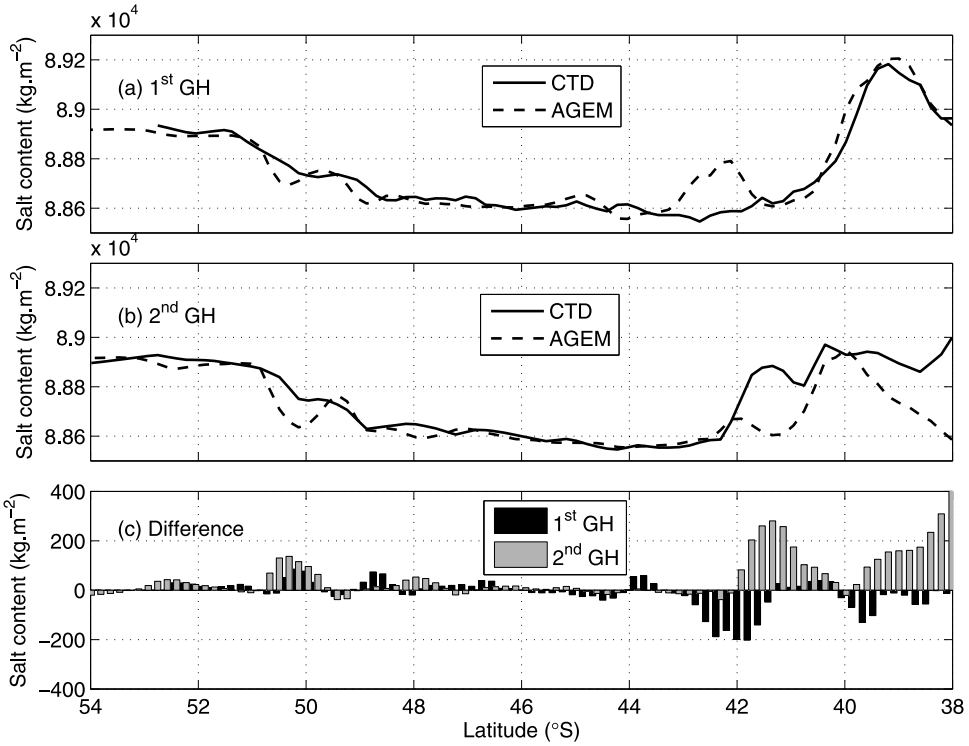


**Figure 3.** Comparison between observed (solid curve) and AGEM-estimated (dashed curve) salt content between the surface and 2500 dbar for the (a) first and (b) second GH occupations. (c) The difference between the hydrographic and AGEM estimates (bars) are summarized, where black bars are for the first occupation and the gray bars are for the second occupation.

the subsurface thermohaline structure of the water column at the GH transect using the whole altimetry time series.

## 4. Hovmöller Analysis of Heat and Salt Content

[15] The methods presented in section 2.4 are applied to the time series of AGEM-produced sections of temperature and salinity to derive the HC and SC, respectively, between 0 and 2500 dbar, along the latitudinal extent of the GH line. The mean of both HC and SC have been removed from this time series to yield the heat content anomaly (HCA) and salt content anomaly (SCA) estimates within this layer, respectively.

### 4.1. Heat and Salt Content Anomaly

[16] We illustrate the HCA and SCA throughout the upper 2500 dbar of the water column in Figure 4. The positions of the ACC fronts, as determined using altimetry data (refer to Part 1 for methodology), are depicted using solid black lines. For simplification, we make use of the "classical" ACC fronts that have been described previously by *Orsi et al.* [1995] and not the multifrontal structure defined by *Sokolov and Rintoul* [2007a, 2009a, 2009b]. Indeed, the discussion of the heat and salt content behavior for the fewer classically defined fronts is simpler and more robust when associated to large-scale modes of variability compared with a more refined study for each secondary frontal structure. Furthermore, *Swart et al.* [2008] show that each of the most dominant multifrontal structures found in each front region relate to the temperature and salinity criteria of the classical ACC fronts given by *Orsi et al.* [1995].

[17] The STF is characterized by sudden and erratic changes in space from one week to another, which makes its difficult to accurately locate its position using altimetry data. This is because the STF south of Africa and particularly in this region is often only present as a series of Agulhas Rings and eddies [*Lutjeharms and Valentine*, 1988], which pass through the northern extremes of the GH line [*Belkin and Gordon*, 1996; *Swart et al.*, 2008; Dencausse et al., submitted manuscript, 2009]. The positions of the other ACC fronts are more stable in nature [*Lutjeharms and Valentine*, 1984] and can be more accurately defined in horizontal space. A detailed description of the position, standard deviation, and behavior of the ACC fronts, derived using this method, is given by *Swart et al.* [2008] and Part 1.

[18] The behavior of the HCA and that of the SCA are quite different from each other (Figure 4). This is particularly true at the fronts and in the frontal zones. The short-term variability of the SAZ is dominated by the presence of mesoscale eddies and meanders, originating from the STF, and of Agulhas Rings, which arrive from the west or west-southwest. In section 4.2, the short-term variability found in the SAZ is explained in more detail.

[19] Compared with the SAZ, the range of HCA and SCA values are considerably reduced within the APZ. Anomalous events in this region are principally driven by the behavior of the Subantarctic Front (SAF). Figure 5 is used to better understand the mean state of the ACC and fronts in the region of the GH line. The color plot represents the RMS of the MADT data, while the surface geostrophic velocities are shown by the arrows. Topography contours

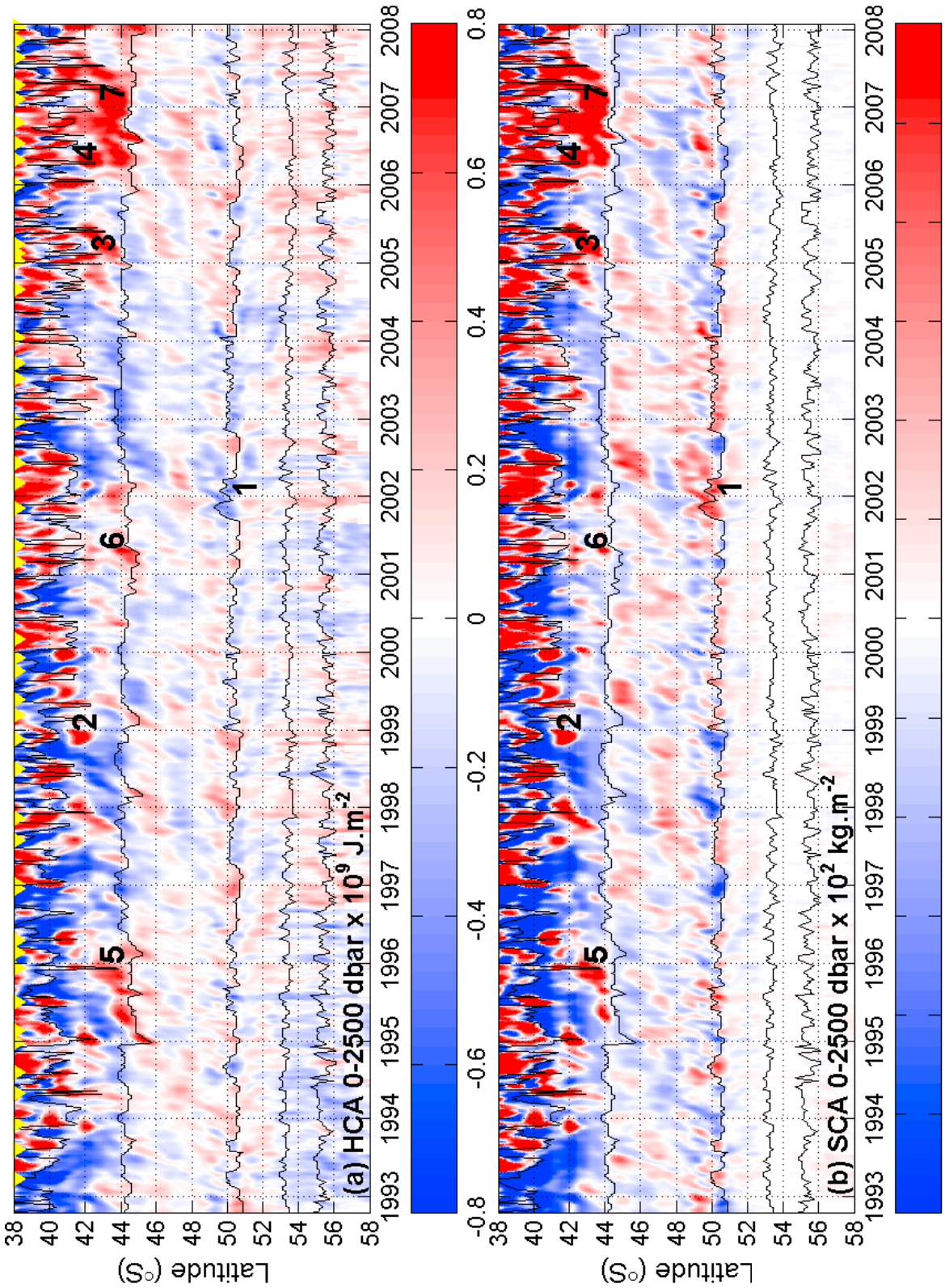


**Figure 4.** A Hovmöller representation of the (a) HCA and (b) SCA between the surface and 2500 dbar, at the GH line from 1992 to 2008. The latitudinal positions of the ACC fronts (thin black lines) are from top to bottom as follows: STF, SAF, APF, SACCF, and SBdy. The number labels are referred to in the text.

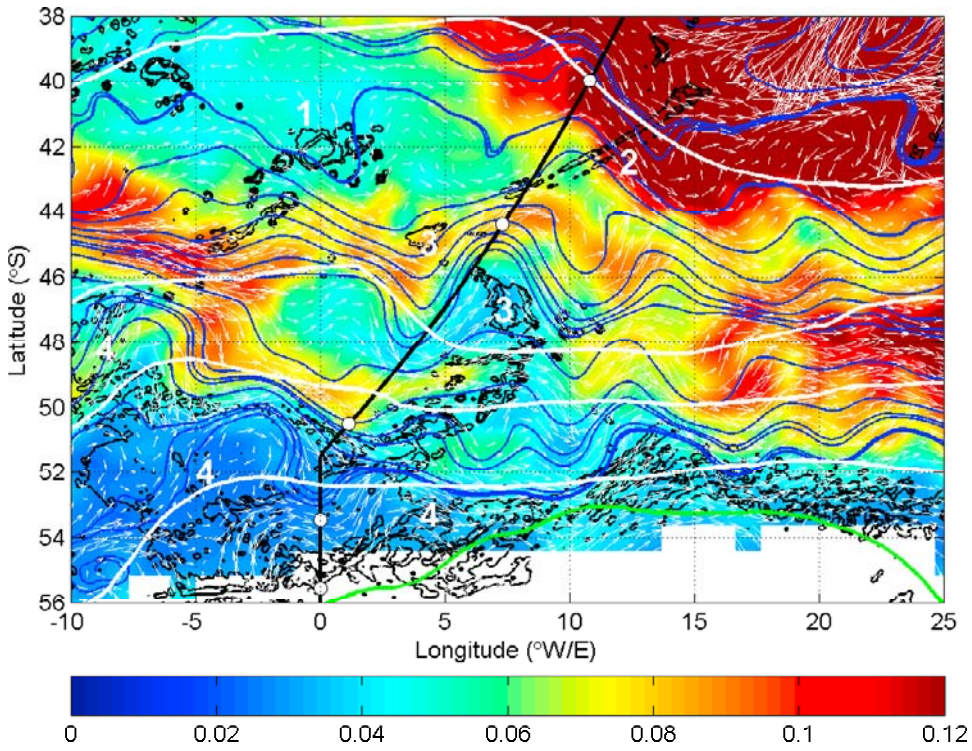


**Figure 5.** The RMS of the MADT (in dyn m) over a 16 year period is shaded in color, while the mean surface geostrophic velocities are represented by the white arrows. The 1000, 2000, and 3000 m bathymetry contours are overlaid (thin black lines) and geostrophic velocity streamlines (blue lines) have been added. The GH line is shown by the thick black line. White spaces represent regions where sea ice was intermittently present during the altimetry time series. The classical ACC fronts, as described by *Orsi et al.* [1995], have been overlaid using solid white curves, apart from the SBdy, which is depicted for clarity as a solid green curve. A white dot located over the GH line depicts the mean front position derived from the time series of MADT data. From top to bottom, these fronts and those of *Orsi et al.* [1995] are as follows: STF, SAF, APF, SACCF, and SBdy. Important bathymetric features are numbered as follows: 1, Discovery Seamount; 2, Agulhas Ridge; 3, Meteor Rise; 4, Mid-Ocean Ridge.

of 1000, 2000, and 3000 m are overlaid and velocity streamlines (blue lines) are also included. In addition, the front positions, given by *Orsi et al.* [1995], have been depicted in the illustration. Apart from the STF, the altimetry derived front positions (Part 1) in Figure 5 do not overlap those derived by *Orsi et al.* [1995] at the GH line. This may be due to some inaccuracies in positioning the fronts using the criteria of *Orsi et al.* [1995]. This is especially the case for the SAF, where recent high-density hydrographic transects have positioned the SAF north of the Meteor Rise [*Ansorge et al.*, 2004; *Gladyshev et al.*, 2008; *Swart et al.*, 2008].

[20] Subsequent to crossing the Mid-Ocean Ridge, the SAF experiences some fragmentation downstream possibly due to a loss of the strong topographic control that could be caused by the meridional steering of the flow by underlying bathymetry and, thereby leading to the genesis of meanders and eddies [*Hogg and Blundell*, 2006]. These perturbations are carried southward due to a meridional shift in the SAF upon reaching the Meteor Rise at 2°E (see Figure 5), thereby distributing anomalous features, in a band, between 46 and 48°S. The SCA in the APZ are opposite in sign to the HCA. This is because mesoscale anomalies originating from the SAF propagate south, carrying with them low salinity intermediate waters of which the mean salinity is considerably lower than the surrounding Circumpolar Deep Water (CDW) found further south. This produces negative SCAs when integrated through the upper 2500 dbar water column and emphasizes the fact that these features originate from regions further north. If we investigate the SCA solely in the upper 400 dbar (not shown), interestingly, the variability in the APZ, is overwhelmingly dominated by the mesoscale anomalies discussed above and indicate their confinement to the upper 600 dbar. Besides the presence of these features, the APZ is almost absent of anomalous episodes of salt content in the upper 2500 dbar.

[21] The high-frequency variability in the HCA and SCA, located in the region of the APF and shown in Figure 4, is quite striking. These events typically last in the order of approximately 8 weeks, while some large events can subsist for up to one year (such as the cool, saline event beginning in mid-2001; labeled "1" in Figure 4). This form of variability is characteristically mesoscale in nature and we now attempt to provide evidence for this statement.

[22] Referring to Figure 5, the impeding Mid-Ocean Ridge, at 50°S; 10°W, exerts strong topographical control over the path of the APF and forces the mean geostrophic

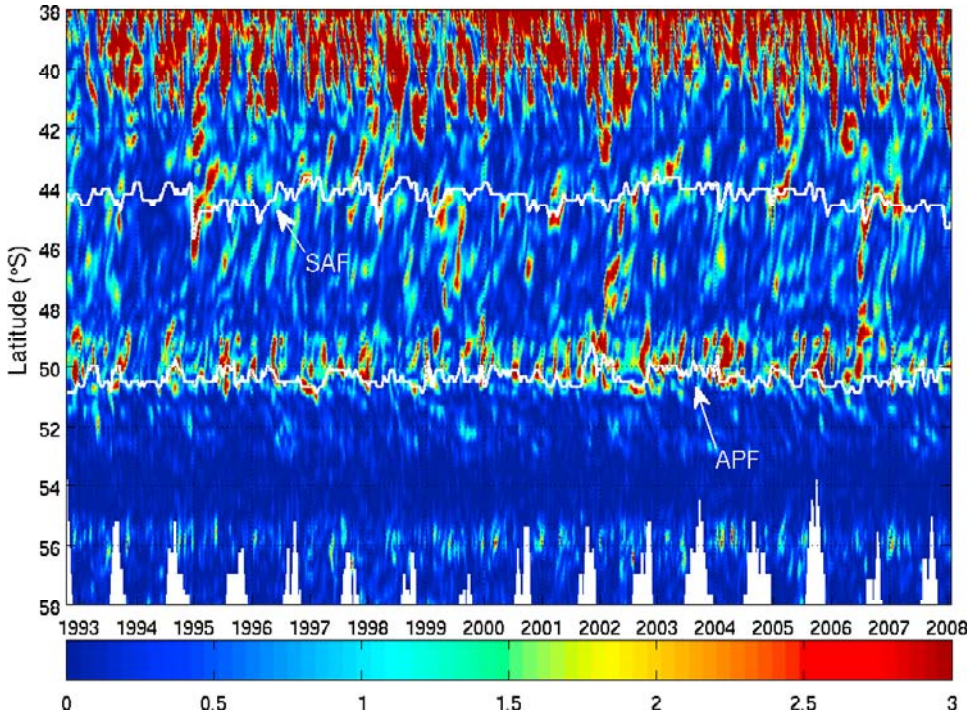


**Figure 6.** A Hovmöller representation of the surface eddy kinetic energy at the GH line from 1992 to 2008. The latitudinal positions of the SAF and APF, determined using altimetry data, are overlaid (white lines).

flow northward. This is as a result of the flow being forced across isolines of planetary vorticity, which causes an input of relative vorticity to the water column by the shrinking of vortex lines [*Moore et al.*, 1997, 1999] due to the decrease in depth. Further downstream, the APF follows contours of $f/h$, roughly along the edge of the 2500 m isobath before a loss of topographic control occurs prior to reaching the GH line. Downstream of the Mid-Ocean Ridge, this input of relative vorticity is likely balanced through nonlinear processes such as eddy genesis and Rossby waves [*Hughes*, 1995, 1996]. Thus, elevated mesoscale variability is found in this region resulting in the band of mesoscale-type signals found in the HCA and SCA. This evidence is supplemented by the existence of a branch of elevated MADT RMS extending over the GH line in Figure 5. This high level of RMS associated with the APF is also shown by *Moore et al.* [1999] who explain that the position of the APF varies significantly (and therefore is unstable) at the Greenwich Meridian, subsequent to crossing the Mid-Ocean Ridge.

[23] South of the APF, the SCA variability in the upper 2500 dbar, is considerably lower. This is because the variability present at the surface is dampened by the monotonic salinity structure below the halocline, which is located between 200 and 300 dbar. If we remove the majority of the relatively high saline, monotonic layer by computing the SCA between the surface and 400 dbar (not shown), we are able to reveal the true SCA variability in the upper ocean layer. A large portion of the temporal variability of salinity, between the APF and southern boundary of the ACC (SBdy), originates in the mesoscale band. Additional interannual signals in the variability can be seen in both the HCA and SCA and will be discussed in section 5.1 using time series analysis.

[24] Elevated eddy kinetic energy (EKE) has been noted downstream of major topographic features [*Daniault and Menard*, 1985; *Patterson*, 1985; *Chelton et al.*, 1990; *Morrow et al.*, 1994]. The kinetic energy budget at the GH line is illustrated to emphasize this point. The deviations of $u'$ and $v'$ from the mean $(\overline{u}, \overline{v})$ allow one to estimate the EKE per unit mass

$$EKE = \frac{1}{2}\left(u'^2 + v'^2\right). \tag{3}$$

The kinetic energy, per unit mass, of the mean flow is referred to as the mean kinetic energy (MKE) and is defined by *Richardson* [1983]

$$MKE = \frac{1}{2}\left(\overline{u}^2 + \overline{v}^2\right). \tag{4}$$

A Hovmöller diagram representing the anomaly of the surface EKE along the meridional extent of the GH line (Figure 6) highlights the behavior of the kinetic energy expected to be produced by the passage of mesoscale meanders and eddies in the region of the APF, while to the north a wider and less defined band of elevated EKE depicts the SAF. Furthermore, this illustration clearly indicates the intensity of the EKE magnitude difference between the extremely active mesoscale region associated with the subtropical domains and passage of Agulhas Rings with that of the major ACC fronts beginning just a few degrees further south (to be discussed further in section 4.2). In some instances, the ring structure of the most southern propagating Agulhas Rings can be made out in Figure 6. The distribution of the mean surface kinetic energy budget, at the GH line, is shown in Figure 7. This clearly highlights

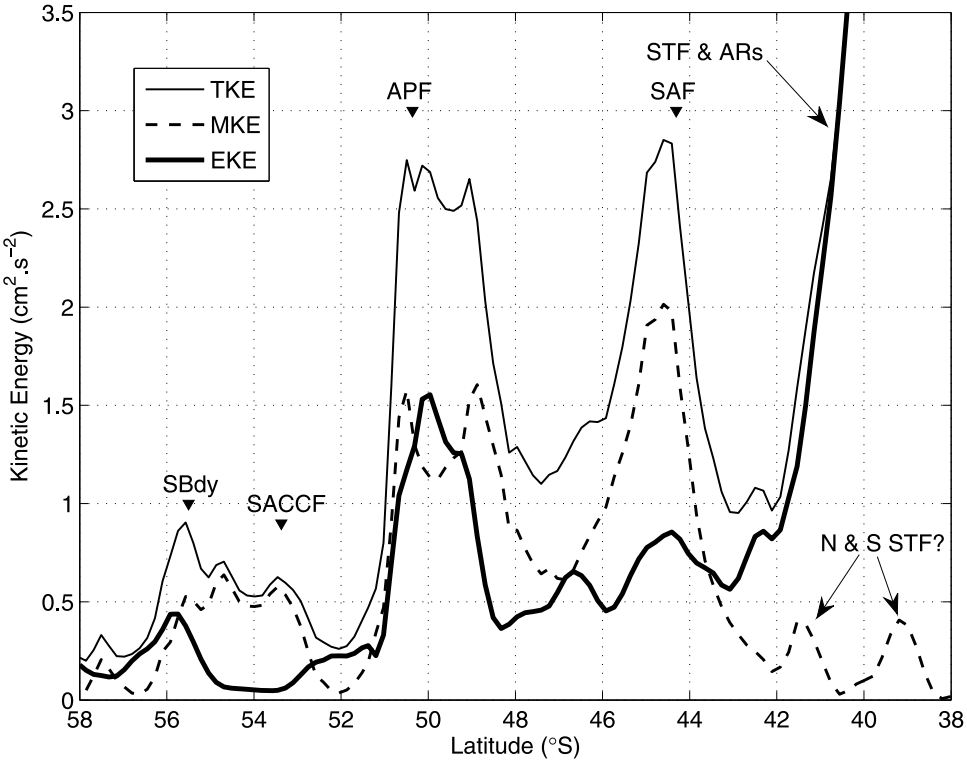


**Figure 7.** The latitudinal distribution of the 16 year mean surface kinetic energy at the GH line is separated into the total kinetic energy (thin solid curve), mean kinetic energy (dashed curve), and eddy kinetic energy (thick solid curve). The mean positions of the ACC fronts, determined using altimetry data, are indicated by the arrows. The abbreviation "ARs" stands for "Agulhas Rings."

the different behavior of the SAF and APF. At the SAF, the largest contribution to the total kinetic energy (TKE) comes from the mean kinetic energy (MKE), which is the kinetic energy related to the time and zonal mean motion, likely due to the topographic steering caused by the Meteor Rise that creates a zonal-dominant jet at the crossing of the GH line. To the contrary, the EKE is particularly high at the APF (double the EKE at the SAF; >1.5 cm$^2$.s$^{-2}$) when compared with the rest of the ACC south of the STF. This is likely as a result of the meridional-type motion caused by the passing of eddies, generated on an almost continual basis, while the MKE at the APF, downstream of the Mid-Ocean Ridge, is approximately 0.5 cm$^2$.s$^{-2}$ less than at the SAF. The southern ACC front (SACCF) and the SBdy are also represented in the kinetic energy budget. The SACCF is largely dominated by the MKE, suggesting little mesoscale variability in the mean flow, while the EKE is considerably higher at the SBdy, symptomatic of increased mesoscale activity. The EKE at the region around the STF is disproportionately higher than the MKE, which is as a result of the intense mesoscale activity found at the unstable STF, largely due to the passage of Agulhas Rings. Remnants of the mean position of the northern and southern branches of the STF are likely represented by the elevation of MKE at 39°S and 41.5°S, respectively.

### 4.2. Dominant Forcing of Dynamic Variability in the SAZ

[25] Extensive analysis of MADT data, in conjunction with both the HCA and SCA time series, are used to identify two dominant aspects that force the variability within the SAZ. These dominating aspects are first the westward or west-southwestward propagating Agulhas Rings into the SAZ and the second is eastward propagating eddies that have their origin in the unstable STF upstream (west) of the GH line. A time series of MADT "snapshots" are included to help clarify the following discussion (Figure 8).

[26] The northern parts of the SAZ (40–42°S) are subjected to generally short (2 months), yet intense episodes of elevated HCA that occur approximately 2.7 times per year. These episodes are also clearly identifiable as intense peaks in the surface EKE, illustrated in Figure 6. On some occasions, these anomalous features can remain in the region for extensive periods of time (up to 14 months). These features are identified as Agulhas Rings using MADT data by backtracking their trajectories to confirm their origins are within the Agulhas Retroflection region (see Figure 8). Confidence in this form of analysis is further given by *Swart et al.* [2008] who matched the Agulhas Rings, identified in the MADT data, with in situ XBT sections in order to describe their vertical temperature structure. In total, 43 individual Agulhas Rings are located in the MADT data and seen crossing the GH line between 40 and 43°S, during the 16 years of available data. Three Agulhas Rings that are found quite far south in the SAZ, are identified in Figure 4 by labels "2," "3," and "4." During these instances, the HCA at a single vertical profile increases to >2.3 $\times$ 10$^{10}$ J m$^{-2}$. The frequency of their presence in the SAZ is not always uniform, as shown by an

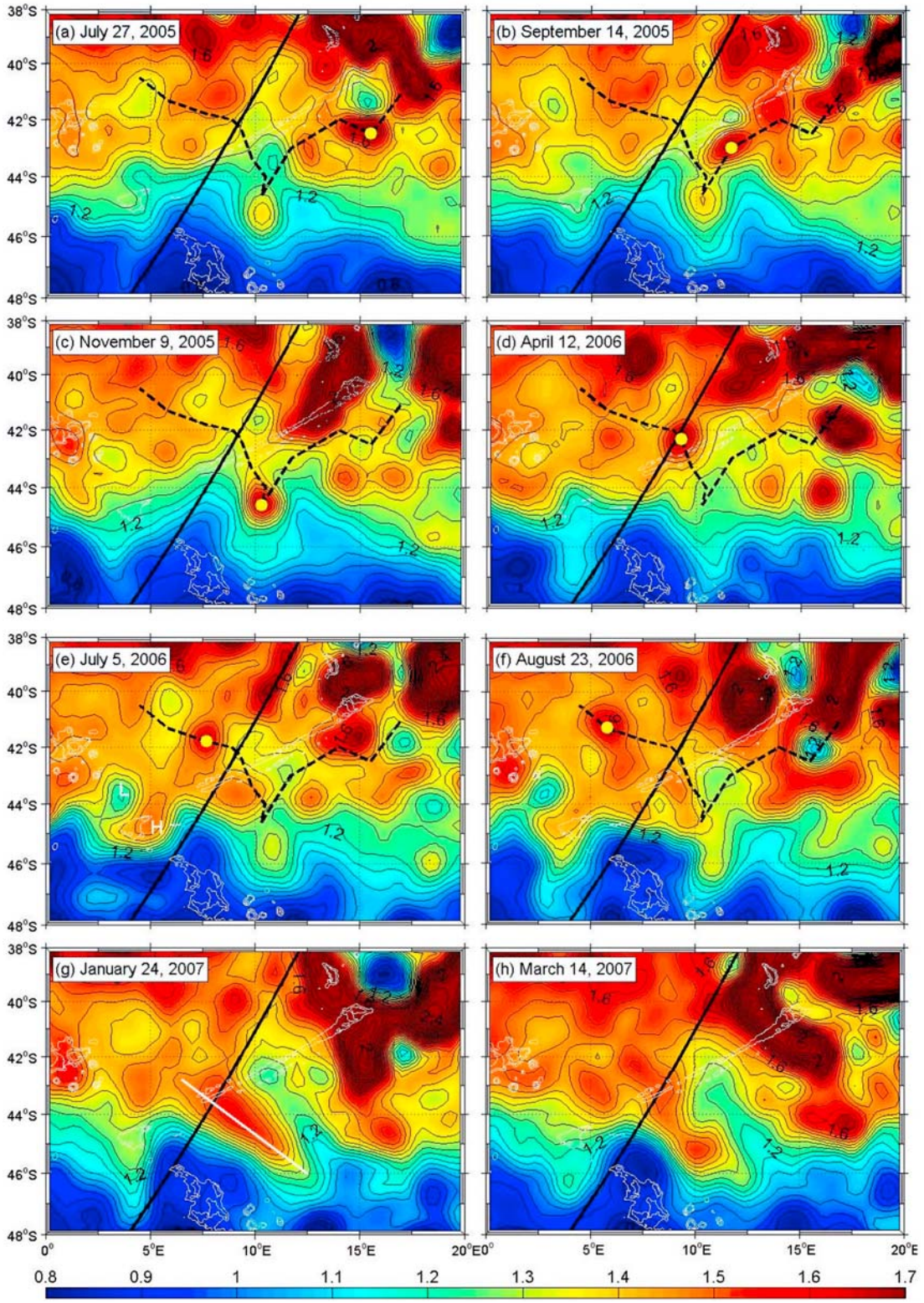


**Figure 8.** (a–h) A sequence of maps between 27 July 2005 and 14 March 2007 illustrating the weekly MADT data (in dyn m) for the region near the GH line. The propagation of an Agulhas Ring is identified with a yellow dot near its core. The black dashed curve, in Figures 8a–8f, represents the approximate path (from east to west) of the Agulhas Ring between 13 July 2005 and 6 September 2006. The GH line is marked by the thick black curve and topography for the region (1000, 2000, and 3000 m isobaths) is marked with thin white lines. The dynamic height values have a contour interval of 0.05 dyn m. The thick white line in Figure 8g depicts the approximate length of the warm anomalous feature described in section 4.2.

**Table 2.** Comparison Between the Mean Hydrographic State and the Average Hydrographic State When Agulhas Rings Are Present in the SAZ[a]

| | Temperature Surface (°C) | Temperature 200 dbar (°C) | Salinity Surface (psu) | Salinity 200 dbar (psu) | Diameter (km) |
|---|---|---|---|---|---|
| Mean hydrographic state | 10.6 | 8.8 | 34.48 | 34.52 | – |
| Agulhas Ring | 15.7 | 12.4 | 35.24 | 35.24 | 190 |
| Standard deviation | 0.73 | 0.77 | 0.13 | 0.13 | 60 |
| Difference | 5.1 | 3.6 | 0.76 | 0.76 | – |

[a]Mean hydrographic state from 1992 to 2008. The standard deviation for the 10 sampled Agulhas Rings is shown.

observation in 1999 when Agulhas Rings are found on four occasions within the SAZ, followed by a quiescent period between May 2000 and January 2001, when no Agulhas Rings are located. To give an indication of their frequency, yellow arrows in Figure 4 indicate the presence of an Agulhas Ring in the SAZ.

[27] The presence of Agulhas Rings south of the STF seem to play a large role in the HCA and SCA of the SAZ. The values of integrated HCA and SCA in the SAZ are isolated during the 43 instances when the Agulhas Rings have their maximum presence in the SAZ (i.e., they are at their most southern extent) and compared to the mean HCA and SCA during the 16 year time series. The mean HCA (SCA) throughout the time series is $-1.9 \times 10^{10}$ J m$^{-1}$ ($-586$ kg m$^{-1}$). The mean HCA (SCA), during periods when the Agulhas Rings are present in the SAZ, is calculated as $2.86 \times 10^{10}$ J m$^{-1}$ (451 kg m$^{-1}$). This shows that the presence of Agulhas Rings in the region increase the HCA and SCA by $4.76 \times 10^{10}$ J m$^{-1}$ and 1037 kg m$^{-1}$, respectively. Additionally, the HCA (SCA) is greater than the mean 80% (82%) of the time an Agulhas Ring is present in the SAZ.

[28] On average, the entire spatial extent of an Agulhas Ring tends to cross the GH line in approximately 56–70 days (or 8–10 weeks), which equates to a propagation speed of $\sim$0.04 m s$^{-1}$. On rare occasions (such as for the feature labeled 2 and 3 in Figure 4) the Agulhas Ring propagates over the GH line at a much reduced speed of $\sim$0.023 m s$^{-1}$ and may take between 90 and 130 days to cross the cruise track. This is approximately 40% slower than the normal propagation speed. The slower propagating Agulhas Rings cross the GH line further south than their faster moving northern brothers. Inspection of the MADT time series shows that the Agulhas Rings located further south are initially occluded from the Agulhas Retroflection slightly further south than the average Ring. This leads to the Agulhas Ring being "trapped" by the shallow topography, associated with the Agulhas Ridge (centered at $\sim$42°S; 13°E and $\sim$2000 m deep at its shallowest), thereby considerably slowing its propagation speed. The Agulhas Ring then moves over the Agulhas Ridge and continues on its northwestward path, and on its way it crosses the GH line, located approximately 3° west of the Agulhas Ridge (see Figure 5 for bathymetry references).

[29] Ten average size and average behaving Agulhas Rings, that crossed the GH line in the SAZ, are further analyzed to estimate their hydrographic impact on the region. This is undertaken by comparing the Agulhas Rings mean hydrographic state to the 16 year mean hydrographic state of the SAZ, at the average location where Agulhas Rings cross the GH line. These results are summarized in Table 2. Note also that when an Agulhas Ring is present, the

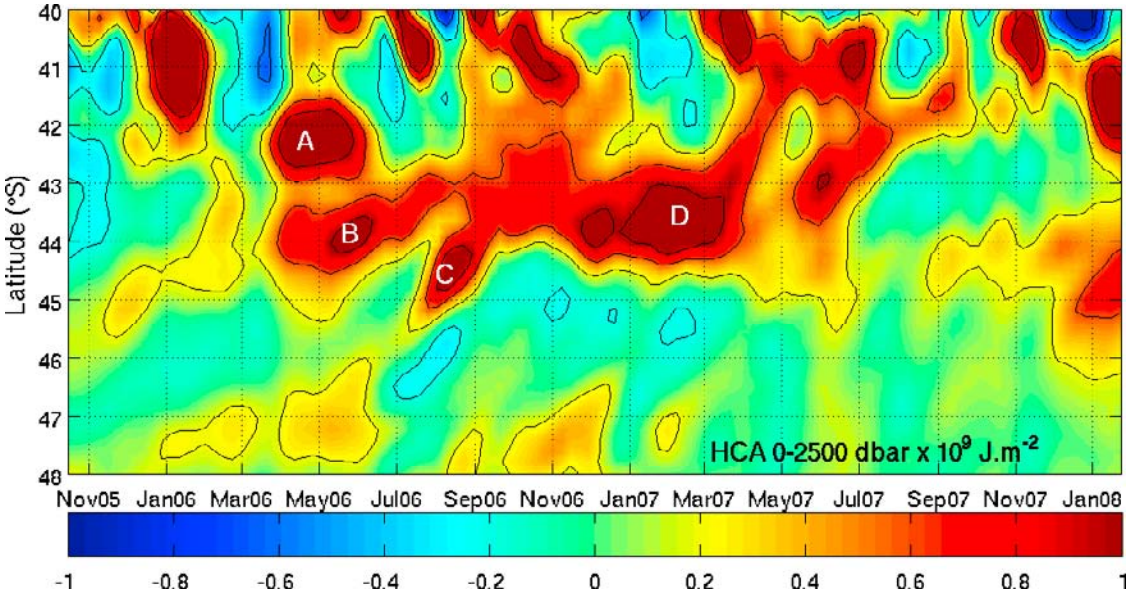


**Figure 9.** A Hovmöller representation of the HCA between the surface and 2500 dbar, at the GH line, focusing on an anomalous feature found roughly between April 2006 and September 2007. The letter labels given are described in section 4.2.

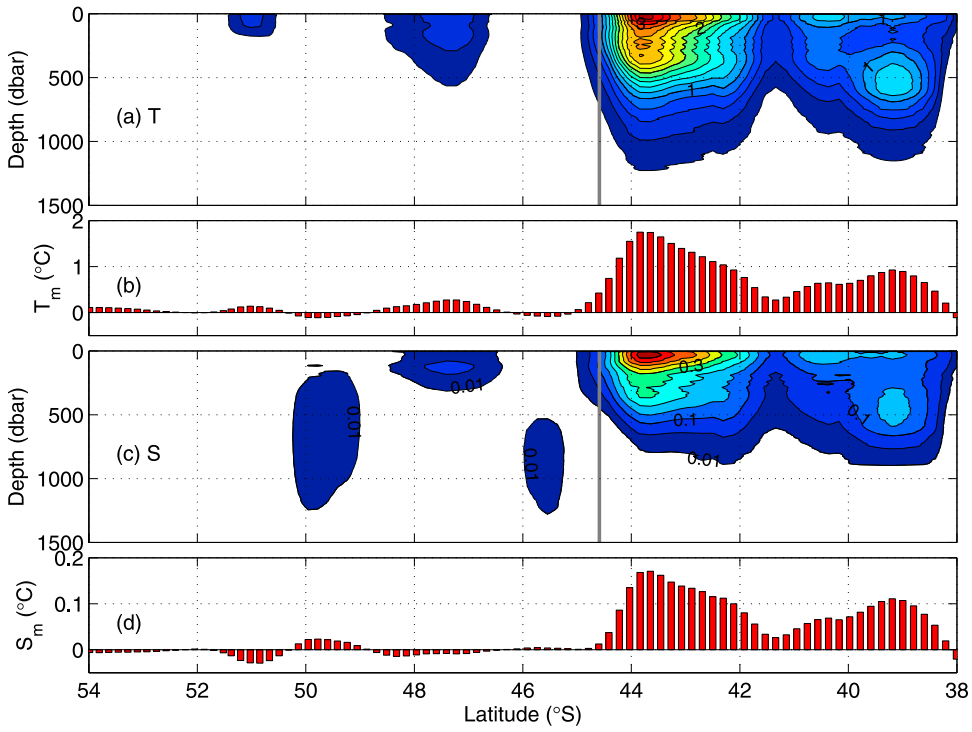


**Figure 10.** The anomalous subsurface structure of (a) temperature and (c) salinity for the anomaly evident in Figure 9 is shown for the period between March 2006 and March 2007. The anomalous (b) temperature and (d) salinity is averaged between 0 and 1000 dbar. The gray line indicates the position of the SAF during the time when the anomalous feature was present. The contour intervals are 0.2°C and 0.05 psu for the temperature and salinity anomaly plots, respectively.

temperature (salinity) at the surface and at 200 dbar increases to 5.1°C (0.76 psu) and 3.6°C (0.56 psu), respectively.

[30] The HCA variability found in the southern parts of the SAZ is forced by mesoscale perturbations in the form of large meanders and eddies that occur within the SAF and SAZ further upstream of the GH line. It is likely that these instabilities are caused following the SAF's path over the Mid-Ocean Ridge at ~44°S; 12°W. A complete analysis of MADT data and its geostrophic velocity component is done to analyze the nature of the positive anomalies labeled "5" and "6" in Figure 4. Preceding these warm events, the MADT data shows the formation of a large meander in the SAF upstream of the GH line (not shown). In some cases, this meander may pinch off to form a warm eddy, which carried by the mean easterly flow of the SAF and ACC, propagates downstream. This eddy is then steered quite sharply northward by the rise in topography, associated with the Meteor Rise. The "slanted" spread of positive HCA in the Hovmöller representations (Figure 4), is caused by the feature crossing the GH line from the southwest. Greater detail on the behavior of these anomalous features is described below.

[31] We now attempt to explain the complex nature of the intensely positive HCA and SCA values found in the SAZ, which began in March 2006 and remained in the region until October 2007 (labeled "7" in Figure 4). Figure 9 shows a "zoom" of the HCA, between the surface and 2500 dbar, for this particular event in order to detail its structure more precisely. The initial increase in the HCA (labeled "A" in Figure 9) is caused by an Agulhas Ring crossing the GH line between March and June 2006. A set of MADT snapshots are shown in Figure 8 to identify the Agulhas Ring mentioned here, which for clarity is marked with a yellow dot near its core. The Agulhas Ring propagates in a WSW direction from the Agulhas Retroflection (Figure 8a), seemingly guided by the Agulhas Ridge (Figure 8b) before merging with a warm eddy (centered at 45°S; 11°E) that is positioned on the leeward side of the SAF meander (located over the GH line), thereby intensifying its MADT gradient (Figure 8c). The feature remains quasi stationary at this location for 10 weeks before progressing in a northwest direction and crossing the deepest part of the Agulhas Ridge and then intersecting the GH line in April 2006 (Figure 8d).

[32] Shortly after crossing the Agulhas Ridge (1 month), the Agulhas Ring appears to split into two independent parts (Figure 8e; indicated by label "B" in Figure 9). The northern part continues to advance to the northwest and away from the region, while the southern part is fed by flow originating from the STF, before likely being influenced by the strong mean easterly flow and returning back to the southeast (southeast of the GH line). At approximately the same time as the splitting of the Agulhas Ring, a large meander in the SAF is pinched off to form a warm and cold eddy, labeled "H" and "L" in Figure 8e, respectively. This warm eddy clearly moves downstream and crosses the GH line from the southwest, at the beginning of July 2006 (labeled "C" in Figure 9). This eddy merges with the already present southern portion of the Agulhas Ring resulting in an intense, elongated anomaly that consequently produces elevated HCA and SCA values in the region for

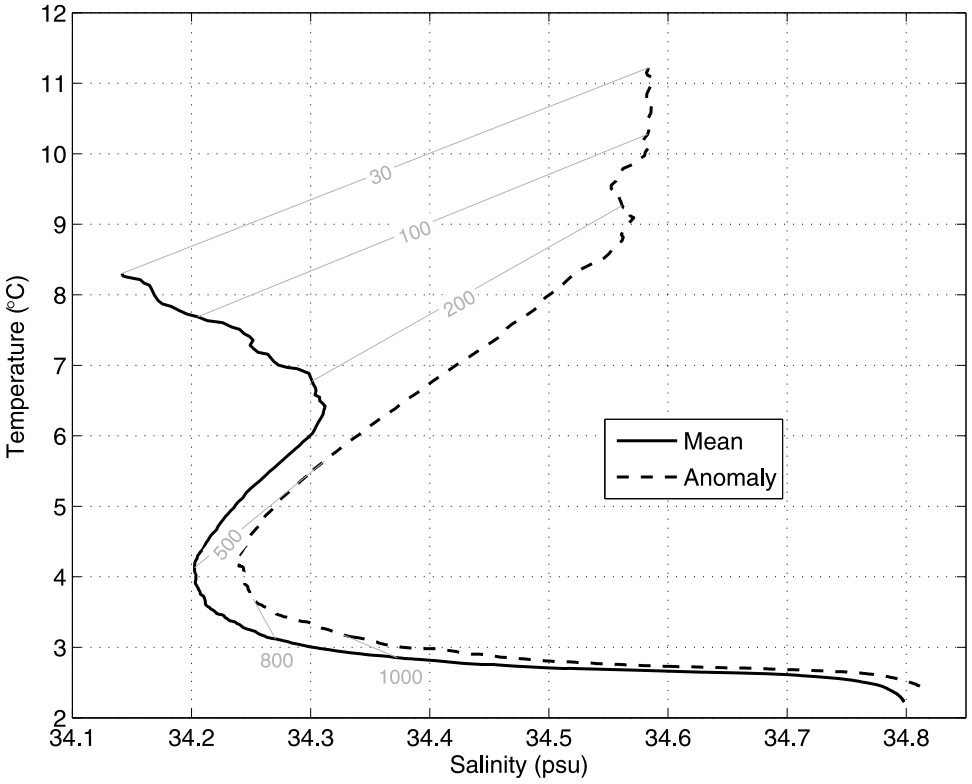


**Figure 11.** An AGEM-derived T-S diagram for a locale at 43.8°S indicating the 16 year mean structure (solid curve) and for the period when the anomalous feature was present between March 2006 and March 2007 (dashed curve). The gray lines connect values of equal depth.

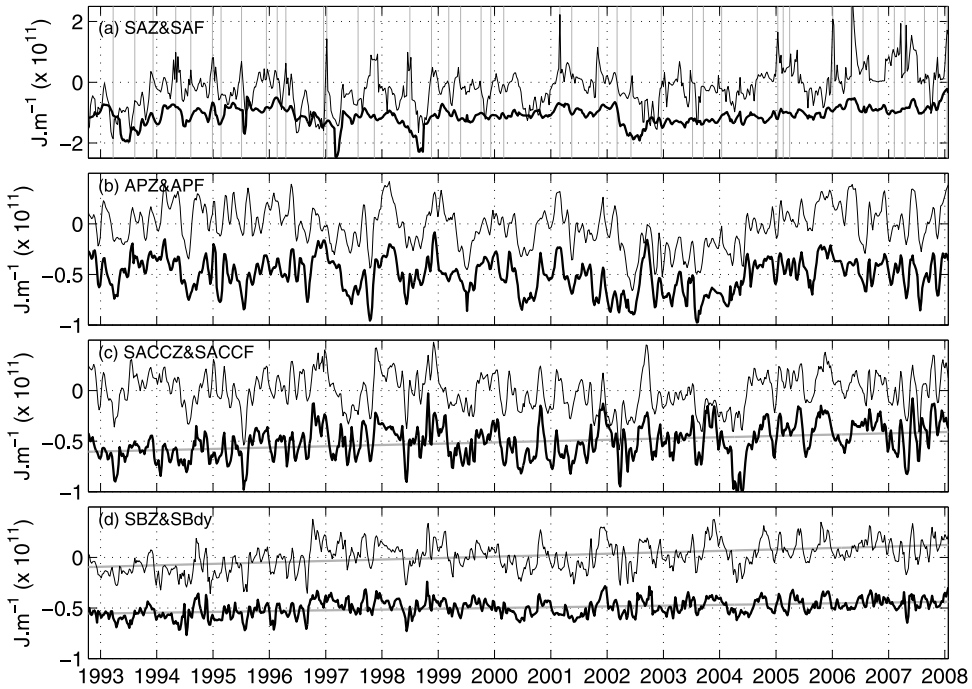


**Figure 12.** The time series of HCA is shown for each frontal zone (thin curve) and each ACC front (thick curve): (a) SAZ and SAF, (b) APZ and APF, (c) SACCZ and SACCF, and (d) SBZ and SBdy. The presence of an Agulhas Ring in the SAZ is marked by the gray lines in Figure 12a. The gray lines in Figures 12c and 12d mark the trends in HCA for the respective fronts and frontal zones.

approximately one year (November 2006 to October 2007; labeled "D" in Figure 9). The feature has a maximum length of 950 km and width of 220 km. At its peak intensity in February 2007, this feature elevates the HCA at an individual vertical profile to $1.4 \times 10^9$ J m$^{-2}$ and the SCA to 320 kg m$^{-2}$.

[33] The time series of GEM-produced hydrographic sections are used to analyze the anomalous temperature and salinity subsurface structure associated with this positive feature. The mean temperature and salinity between March 2006 and March 2007 are subtracted from the mean for the whole period (16 years) and shown in Figures 10a and 10c, respectively. Over this period, the maximum anomalous temperatures and salinities occur near the surface and are approximately 3°C and 0.5 psu above the mean, respectively. A localized subsurface maximum is associated with the northern boundary of the Agulhas Ring and found at 500 dbar. The extent of the positive feature reaches roughly 1500 dbar. The latitudinal anomalous temperature and salinity is averaged between 0 and 1000 dbar and shown in Figures 10b and 10d, respectively. At the core of the Agulhas Ring feature the anomalous temperature and salinity exceeds the mean by 1.75°C and 0.17 psu, respectively. The feature appears to be strongly confined in space by the mean position of the SAF at 44.6°S (represented by the gray line in Figures 10a and 10c), as indicated by the strong thermal and saline gradient at its southern edge. This is likely due to the topographic steering of the SAF over the region of the GH line, thereby inhibiting the southward propagation of mesoscale features approaching from the north. A comparison of the T-S properties between the period of the anomalous feature and the 16 year mean depicts the departure of the T-S structure from one another at a fixed geographic position −43.8°S (Figure 11). The deviation is most magnified in the surface waters but can also be clearly portrayed in the central and intermediate waters.

[34] The presence of Agulhas Rings in this region is of particular interest due to the fact that they are able to transport large quantities of heat and salt from the subtropics to the SAZ, as well as that these features can remain in the region for as long as 14 months. The influence they may have on the local biology and biogeochemistry structure of the region is yet to be understood and warrants further research.

## 5. Heat and Salt Content Time Series

[35] In order to quantify the observed variability in the ACC, we estimate the integrated HCA and SCA in the following ways (only the integrated HCA is shown in this study): (1) the property integral between fronts, defined using altimetry, to derive the value for the frontal zones (thin curves in Figure 12) and (2) the property integral between the northern and southern limit of each front to derive the value for the core region of the front (thick curves in Figure 12). These two integral methods allow us to understand the variability occurring between each front, which may be a contribution to frontal heat and salt exchange in the Southern Ocean as well as the variability occurring within the core of each jet and therefore the manifestation of variability in the zonal-dominant mode of the flow and the behavior of the front. Note that the northern and southern limits of each ACC front have been taken from *Swart et al.* [2008] and a brief explanation has been given in section 2.3.

### 5.1. Time Series and Wavelet Analysis

[36] The continuous wavelet transform (CWT) has been extensively used in time series analysis of geophysical parameters within the last ten years. It is well adapted to the study of multiscale, nonstationary phenomena occurring over finite spatial and temporal domains [*Lau and Weng*, 1995] and has been applied in meteorological and oceanographic studies to indicate modes of variability, such as the El Niño Southern Oscillation. *Torrence and Compo* [1998] and *Daubechies* [1992] provide a practical guide to wavelet analysis and more detailed explanations on its application to geophysical data. The Fourier Transform is not utilized in this study as it does not contain any time dependence of the signal and therefore cannot provide local information regarding the time evolution of its spectral characteristics [*Lau and Weng*, 1995].

[37] The CWT allows for the decomposition of a signal $x(t)$ into elementary contributions localized in time and in frequency using mathematical tools, called wavelets. These wavelets are obtained from a single function $\Psi$ by translations and dilations

$$\Psi_{b,a}(t) = \frac{1}{a}\Psi\left(\frac{t-b}{a}\right), \tag{5}$$

where $a > 0$ is the dilation parameter and $b$ is the time translation parameter. The CWT expands the time series into a two-dimensional parameter space ($b$, $a$) and yields a measure of relative amplitude of local activity at scale $a$ and time $b$ [*Melice et al.*, 2001]. More specifically, the Morlet wavelet is used in this study because it is best suited for analysis of geophysical data sets [*Lau and Weng*, 1995]. The Morlet wavelet is a complex exponential modulated by a Gaussian function

$$\Psi(t) = \pi^{1/4} e^{-t^2/2} e^{i\omega_0 t}, \tag{6}$$

with $i = (-1)^{1/2}$ and where $\omega_0 = (2/\ln 2)^{1/2}$ [*Daubechies*, 1992] is chosen to be large enough to ensure that $\psi(t)$ satisfies the admissibility condition, which practically is equivalent to

$$\int_{-\infty}^{\infty} \Psi(t)dt = 0. \tag{7}$$

By inverting the modulus scale, the wavelet becomes a time frequency analysis where the dilation parameter $a$ corresponds to the period and the translation parameter $b$ corresponds to the time.

[38] First, we analyze the time series of the integrated HCA (Figure 12) and SCA in each frontal zone at the GH line. The choices of wavelet figures displayed in this paper are those that are of most interest and/or contribute to explaining the largest proportion of the observed variability.

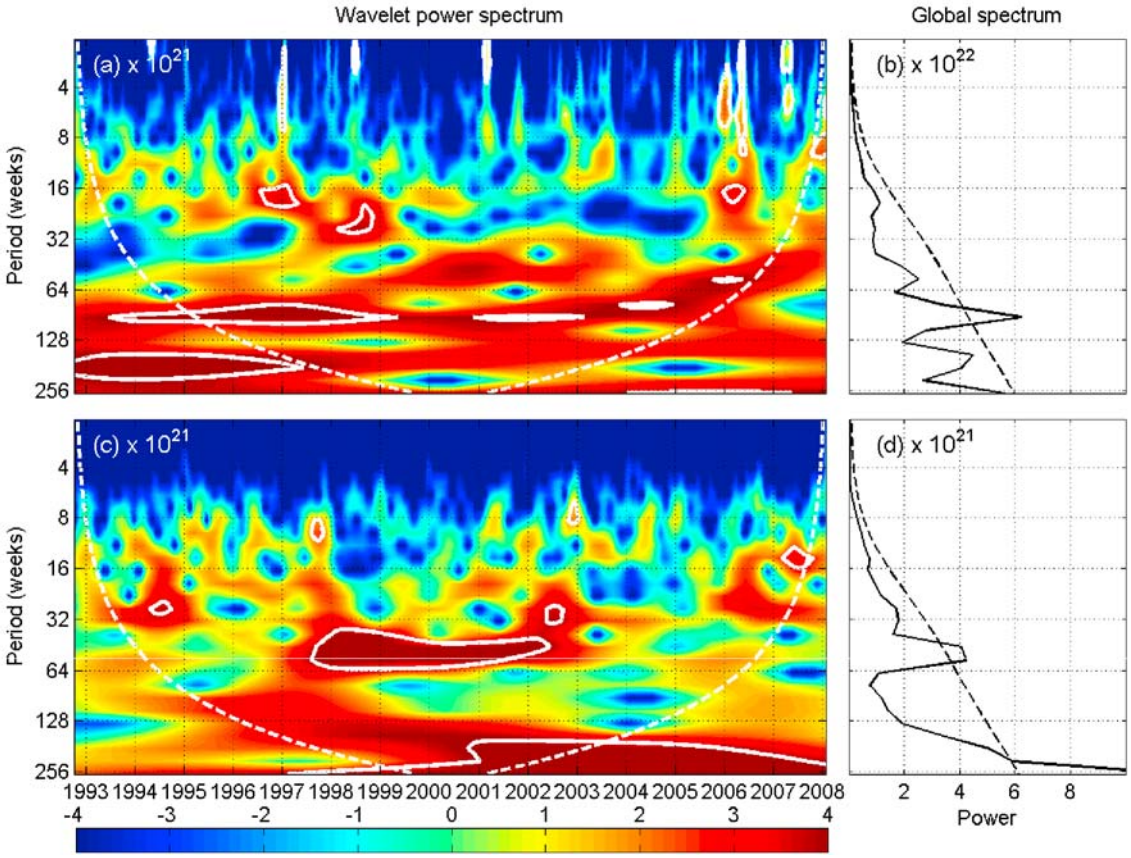


**Figure 13.** The modulus of the wavelet transform, using the Morlet wavelet, is shown for the (a) SAZ and the (c) APZ. The mean power of the global spectrum (solid curve) with the 95% significance level indicated (dashed curve) is shown for the (b) SAZ and (d) APZ. White contours in Figures 13a and 13c indicate where the wavelet amplitude is significant at the 95% level, while the white dashed curves represents the cone of influence.

[39] Agulhas Rings are partially a source of the high-frequency variability experienced in the SAZ and are well resolved in the time series. These events have been previously described in detail in section 4.2. The Agulhas Rings can increase the total SAZ HC and SC up to $1.4 \times 10^{11}$ J m$^{-1}$ and $5 \times 10^{3}$ kg m$^{-1}$ in the upper 2500 dbar, respectively. Some of these events stand out as isolated peaks in the time series due to their extraordinary intensity (such as the Agulhas Ring, which crossed the GH line between March and June 2006). Although the mean wavelet power spectrum, for the periods representing these events, is below the 95% significance level, the wavelet modulus (Figure 13a) does appear to show an increase in amplitude at the period at which the Agulhas Rings appear in the SAZ (2.7 occasions per year or at a period of 20 weeks). Throughout the HCA and SCA time series, the SAZ contains variability that has a period of approximately 80 weeks or 1.5 years, which is well above the 95% significance level, as indicated in Figure 13b. Variability with this period is limited to the SAZ alone. The Hovmöller representation of the HCA in Figure 4a shows that this period appears to be related to the changing positive to negative phases in the HCA and SCA in the central parts of the SAZ. The strong links this region appears to have with the southwest Indian Ocean Gyre (passage of Agulhas Rings) may strongly suggest that the origins of variability on this time scale lie within the subtropics. However, to date this remains unclear.

[40] The variability of the frontal zones is often quite different from that found at the fronts. At the SAF, for instance, the short-term variability (integrated HCA STD = $3 \times 10^{10}$ J m$^{-1}$) is considerably reduced compared with the SAZ (STD = $6.2 \times 10^{10}$ J m$^{-1}$). This is because the influence of Agulhas Rings and other mesoscale variability, associated with the STF, does not penetrate extensively south of the northern branch of the SAF. This may be because the strong baroclinic shear at the front acts as a boundary that blocks the southward propagating mesoscale features that induce the 4 to 12 week scale variability found further north.

[41] The most significant form of variability in the SAF has a period of 5 years and is clearly depicted in the wavelet analysis as a continuous band in the modulus and a statistically significant peak in the mean spectrum (not shown). This pattern is characterized by a slow increase (decrease) in the HCA (SCA) over 4–6 years, followed by a sharp decrease (increase), which takes place over a relatively short time (<1 year). These events are unlikely related to the periodicity/intensity of features originating from north of the SAF because the SCA is of opposite sign to the HCA, which is not indicative of southward displacement of water masses

**Table 3.** Variance Contribution of the Seasonal Cycle to Each Frontal Zone and the Variance Contribution of Each Frontal Zone to the Total Variance of the ACC for Both HC and SC

| Frontal Zone | HC Seasonal Variance (%) | SC Seasonal Variance (%) | HC Variance Contribution to ACC (%) | SC Variance Contribution to ACC (%) |
|---|---|---|---|---|
| SAZ | 9 | 12 | 55 | 65 |
| APZ | 12 | 7 | 18 | 20 |
| SACCZ | 11 | 14 | 16 | 14 |
| SBZ | 19 | 19 | 12 | 1 |

from subtropical origins. However, the short extreme negative episodes in the HCA during mid-1995, early 1997 and late 1998 are of the same sign as the SCA.

[42] The nature of the HCA and SCA time series variability found in the APZ and in the APF are similar and so the description given here is representative for both regions. The short-term variability (in the order of 8 weeks) is dominant in the HCA and SCA time series (Figure 12b), while the wavelet modulus representing the HCA (Figure 13c), indicates a significant mode at the seasonal scale. Although the seasonal variability is present in the time series (localized peaks at the 52 week period in the wavelet power spectrum for the APZ; Figure 13c), it does not seem to contribute significantly to the observed variability. The differences between the seasoned and deseasoned data sets (not shown) are small compared with the higher-frequency variability found in the APF and APZ. Additionally, a new wavelet analysis was performed on the deseasoned data sets for all regions, which revealed no new significant increases in the wavelet power spectrum. However, seasonal warming and cooling of the upper mixed layer may only marginally impact the dynamic height, referenced to 2500 dbar, thus translating to weak HC and SC signals. For this reason we are unable to accurately quantify seasonal variations but we can still provide an estimate as to which regions may undergo larger seasonal variations in comparison to their overall variability. Ongoing work hopes to evaluate, in more detail, the significance the seasonal changes have on the total variance in the region.

[43] Apart from the seasonal cycle, variability with a period of 5 years (or 250 weeks) was found to be well above the 95% significance level in the mean wavelet power spectrum for the APZ (Figure 13d). This cycle can also be seen in the time series (Figure 12b) as a period of slow increasing and decreasing values around three long-term peaks (nadirs) in the HCA (SCA). The maximum peaks occur at approximately mid-1995, early 2001 and early 2006. Unfortunately, the length of the time series means that only three of these cycles can be distinguished and therefore only part of the wavelet power spectrum that is significant is located within the cone of influence (COI).

[44] The mechanism driving this 5 year variability may be linked to the highly nonlinear nature of the ACC dynamics and could be potentially explained by interannual to interdecadal intrinsic variability arising from the meridional topographical steering of the mean flow causing baroclinic instability [*Hogg and Blundell*, 2006]. The role of topographic steering and baroclinic instability on the very rich ACC spatiotemporal spectra has been confirmed by more recent Quasi Geostrophic model simulations [*Thompson*, 2009].

[45] The variance of the HCA and SCA seasonal cycle was compared to the variance of the HCA and SCA time series in other regions in order to evaluate the role the seasonal march may have on the observed variability. The calculated proportion of the HCA seasonal variance

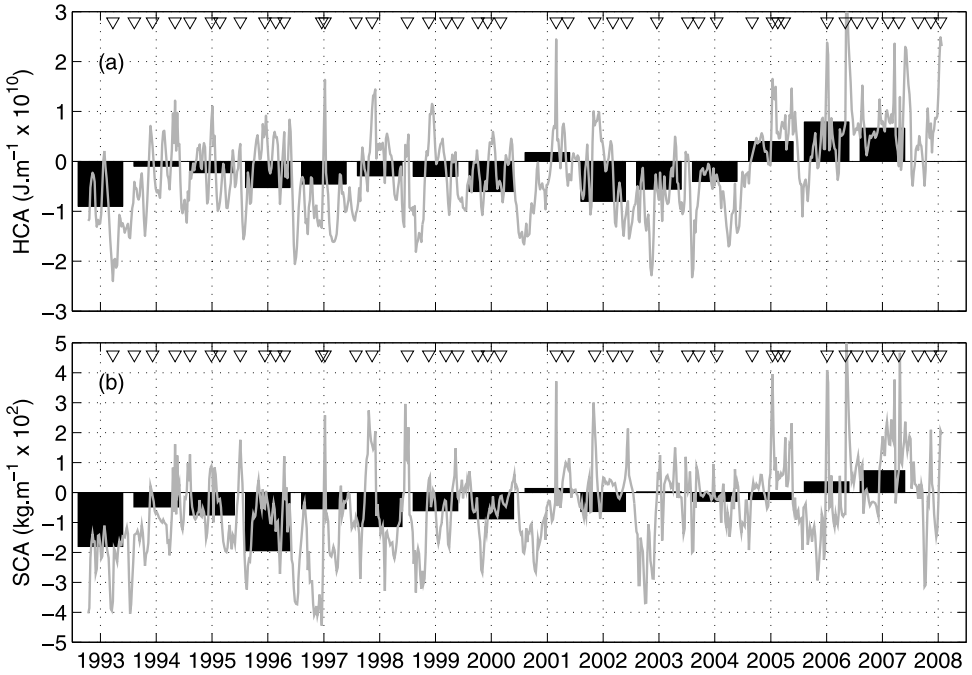


**Figure 14.** The time series of (a) HCA and (b) SCA are shown for the entire ACC domain (gray curves). The annual means are depicted by the bars. The presence of an Agulhas Ring in the SAZ is indicated by the arrows near the upper *x* axis.

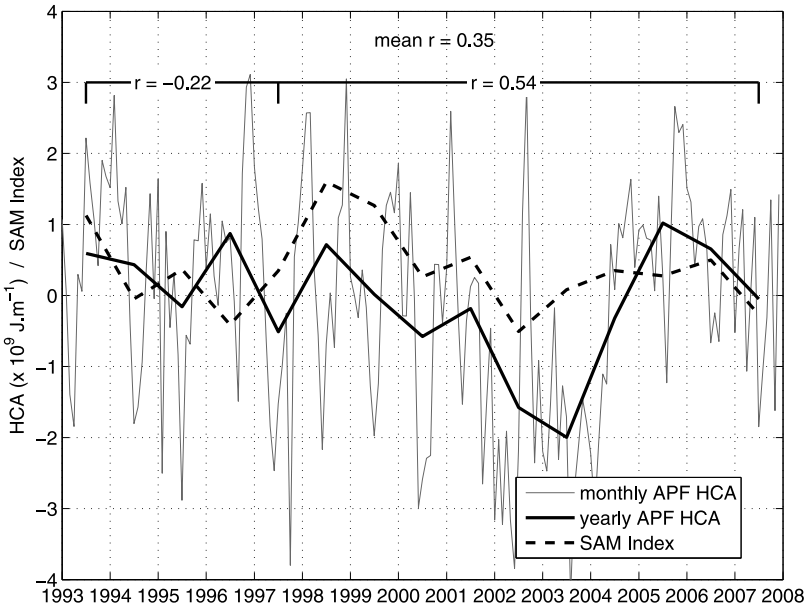


**Figure 15.** The relation between the yearly HCA at the APF (black curve) and the yearly SAM index (dashed curve). The gray curve represents the monthly HCA at the APF. The correlation coefficients are shown for the yearly data sets between 1993 and 1997 and between 1997 and 2008, as well as for the entire time series.

accounted for in the time series, on average, increased poleward and more than doubled between the extreme north of the ACC (SAZ 7%) and the region between the SACCF and the SBdy (hereafter, named the southern boundary zone; SBZ 18%), while the seasonal cycle of SCA progressed southward at a slower rate (SAZ 12%; SBZ 19%). Table 3 provides the percentage contribution of the seasonal variability to the total variance found in the time series of HCA and SCA in each frontal zone.

[46] It is interesting to note that the annual mean time series of HCA depicts short-term positive trends (2004–2007) for all the frontal zones (the annual mean time series of HCA is not shown for each individual frontal zone but only for the entire ACC extent; Figure 14a). The HCA increase in the SAZ may be explained by the intense anomalous feature found in the region at the time (section 4.2). However, as to why the other frontal zones experience a similar gain in HC remains unclear. This is matched by increases in the mean SCA in the SAZ but the SCA decreases in the APZ and the region between the SACCF and the APF, hereafter named the southern ACC zone (SACCZ). This warm period can be seen across the entire meridional extent of the ACC in Figure 4a.

[47] A positive (negative) trend in the HCA (SCA) are found in the southern parts of the ACC (linear trends are displayed in Figures 12c and 12d; not shown for SCA). This is limited to the SACCF, SBdy, and SBZ. These trends are more likely induced by a regime shift, where the HCA (SCA) experiences a rapid increase (decrease) in the final quarter of 1996. In the SACCZ, the mean increase in HCA, between October 1992 and October 1996 and between November 1996 and January 2008, is $1.5 \times 10^{10}$ J m$^{-1}$, while the decrease in SCA is 24.2 kg m$^{-1}$. The positive trends in the HCA seem to be consistent with a southward shift in the southern ACC fronts. Analyses of both altimetry trends in the position of the fronts in this study (not shown [*Sokolov and Rintoul*, 2009b]) and CTD estimates (at the GH line) of frontal positions compared to historical data, show that where the fronts are more free to adjust (i.e., far from steep topography and deep narrow passages), they have had a clear southward shift since the early 1990s (probably due to ongoing climate change). This is especially the case for the subtropical region as well as the southward extent of the ACC and its associated fronts (not shown). Whether these differences are induced by an actual change in the system or by an anomalous spell up until 1997 remains unclear and cannot be answered due to the limited temporal extent of the altimeter time series.

[48] Last, the HCA and SCA are integrated over the entire ACC band (between the SBdy and the STF) and displayed in Figure 14. The SAF and particularly the SAZ are the dominant role players in determining the HCA and SCA variability of the ACC. Clear peaks in both the HCA and the SCA found in the SAZ (Figure 12) are carried over into the ACC variability, while the long-term (5 year) signals can also be detected. The warming and increasing salinity inclination from 2004 to 2008 is emphasized by the annual mean HCA and SCA, respectively. This results in the mean annual HCA and SCA peaking between 2007 and 2008 with values of $0.8 \times 10^{10}$ J m$^{-1}$ and $0.7 \times 10^{2}$ kg m$^{-1}$ above the mean, respectively. A breakdown of the variance contribution of each frontal zone to the entire ACC domain (Table 3) indicates that the SAZ is the dominant variability role player with a 55% (65%) contribution to the HCA (SCA) variance of the ACC. The mean variance contribution of HCA (SCA) declines sharply to 17.5% (20%) for the APZ, 15% (14%) for the SACCZ and 12% (1%) for the SBZ. This strong variance gradient is likely due to the order of magnitude difference in HC and SC found in the Subantarctic region compared with the region south of the APF. Furthermore,

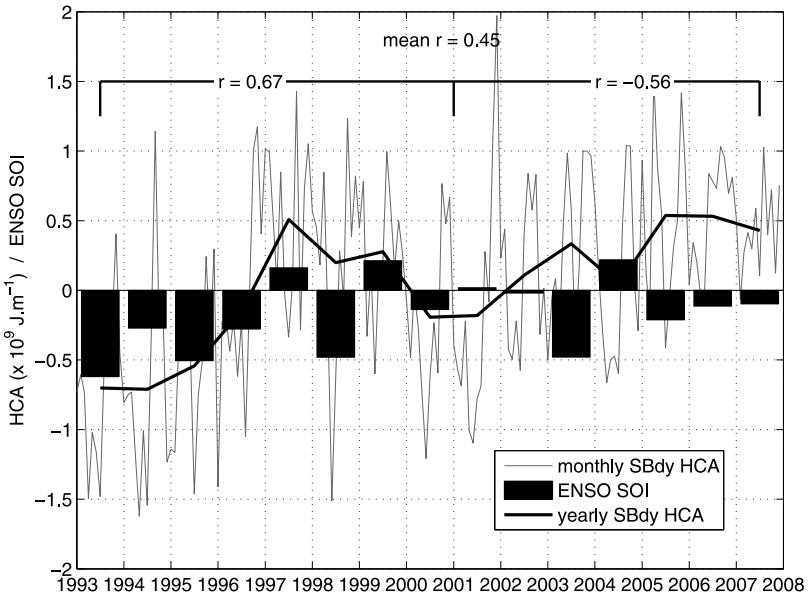


**Figure 16.** The relation between the yearly HCA at the SBdy (black curve) and the yearly SOI (bars). The gray curve represents the monthly HCA at the SBdy. The correlation coefficients are shown for the yearly data sets between 1993 and 2001 and between 2002 and 2008, as well as for the entire time series.

the contrasting strength of the T-S properties associated with mesoscale features originating from the subtropics (e.g., the Agulhas Current and STF) to water masses of the ACC will induce more intense anomalies than those found at higher latitudes. The weak meridional gradients of salinity in the CDW layer dominates the water column below 500 dbar and likely introduces the very low variance in SCA south of the SACCF. The percentage contribution of the variance in each frontal zone to the integrated ACC time series variance is shown in Table 3.

### 5.2. Modes of Variability

[49] This section briefly tests the extent to which the dominant modes of Southern Hemisphere atmospheric variability relate to the observed oceanic variability signals described in this study so far. The weekly time series of HCA and SCA data are used to produce monthly and annual means, for each front and frontal zone, before testing its correlation to the Southern Annular Mode (SAM) index and to the Southern Oscillation Index (SOI). The SAM index, as per *Marshall* [2003], has been incorporated in this study. In short, a true unbiased measure of the SAM has been calculated from the empirical definition of *Gong and Wang* [1999]

$$SAM = P^*_{40°S} - P^*_{65°S}, \quad (8)$$

where $P^*_{40°S}$ and $P^*_{65°S}$ are the normalized monthly zonal mean sea level pressure (MSLP) at 40°S and 65°S, respectively. This has been slightly adjusted to values based on the mean of six station records near each of the two above mentioned latitudes [*Marshall*, 2003].

[50] The SOI is the normalized difference in MSLP between Tahiti, French Polynesia and Darwin, Australia [*Troup*, 1965]. These zonal pressure differences are principally setup by the fluctuations in ocean temperatures during El Niño and La Niña phases [*Rasmusson and Carpenter*, 1982; *Philander*, 1990]. Previous studies have shown that the SOI can strongly affect the Southern Hemisphere atmosphere extratropics, which can in turn allow for an oceanic response [e.g., *Mo and White*, 1985; *Karoly*, 1989; *Mo*, 2000; *Yuan*, 2004].

[51] The relation between the annual means of HCA at the APF and the annual mean of the SAM index (Figure 15) is explained by a correlation coefficient of 0.35 over the full time series. However, the first five years (1993–1997) are found to be anticorrelated ($r = -0.22$), while the remaining part of the time series (1998–2007) shows a relatively strong correlation coefficient ($r = 0.54$) between the two variables. The general trend in the remaining ten years suggests that negative SAM years result in a cooling trend at the APF, and vice versa. The relation between the SAM index and the HCA/SCA in the remaining domains of the ACC do not show a strong connection, with correlation coefficients remaining positive but below 0.26. It may be that the correlation coefficients are higher at the APF because the maximum westerly wind stress occurs here. However, it remains unclear why the correlation coefficients are particularly low in the other ACC regions. These questions are currently being investigated in a study, which hopes to provide a clearer understanding of the relationship between the ACC and the SAM index (W. Billany et al., Variability in Southern Ocean fronts at the Greenwich Meridian, submitted to *Journal of Marine Systems*, 2009).

[52] The SAM index shows a positive summer trend (1957–2005 [*Marshall*, 2003; *Jones et al.*, 2009]) with superimposed anomalies. *Sallee et al.* [2008] suggested that a positive anomaly of the SAM index translates into a southward shift of the APF in the Indian sector of the Southern Ocean. Their definition of the APF is related to a unique value of dynamic height for the entire Southern Ocean and not specific regional values, such as those

defined recently by *Sokolov and Rintoul* [2009b] and in this study, thus they may miss part of the circumpolar variability. For the APF time series derived at the GH line, we see a marked southward shift in the front position. This shift seems to occur more clearly in 1998, with the onset of a positive SAM anomaly (http://jisao.washington.edu/data/aao/ [*Thompson and Solomon*, 2002]). It must be noted that the results of *Sallee et al.* [2008], on the regression of the Sea Level Anomaly onto the SAM index, displays a low correlation for the entire Atlantic sector, suggesting that the imprint of this mode of variability is low in the GH region, compared with the Indo-Pacific sector. On the other hand, *Meredith and Hogg* [2006] suggest a correlation between the SAM index and EKE in the ACC during 2000–2002, which is followed by a 2 year delay relating to the positive SAM anomaly onset of 1998. Furthermore, they explain that the lag is due to the time taken for the SAM to influence the deeper ocean layers. If this increase in eddy activity is related to increases in wind stress (positive SAM anomaly [*Thompson and Solomon*, 2002]) and if the Southern Ocean westerlies have a positive trend, as has been suggested by IPCC simulations [*Cai et al.*, 2003; *Rauthe et al.*, 2004] and various analyses of the NCEP wind field, it may suggest that the positive HCA trend may be explained by an increase in the poleward eddy heat flux [*Meredith and Hogg*, 2006].

[53] The SOI fails to describe any meaningful correlations with the integrated HCA between the STF and SACCF. The SBdy and SBZ, however, do display interesting connections with the SOI with a mean correlation coefficient of 0.45 between the annual mean values of HCA at the SBdy, and the SOI (Figure 16). Notably, if the correlation is performed for the period 1993–2001 the $r$ value increases to 0.67, whereas for the 2001–2007 period, the two time series appear anticorrelated ($r = -0.56$). The reason behind this is not entirely evident but, it suggests a modulation of the mechanism through which the SOI projects into the southern domain of the ACC, east of Drake Passage.

## 6. Discussion and Summary

[54] In this paper, we have studied how to make use of the SSH signal to better understand the role the fronts have in determining the heat and salt content variability of the ACC. This information allows us to determine the finer temporal and spatial component of the variability found at each front and frontal zone of the ACC. The behavior of the variability is noticeably different in each region and is largely a function of subtropical influences and of the underlying topography.

[55] The subtropical-subantarctic dynamical regimes occurring across the GH transect are characterized by the injection of waters to the northwest (for the subtropical region) and to the southwest (for the SAZ) by Agulhas Rings. These features are very intense and are easily detectable using satellite altimetry products. Statistics are now available on the recurrence of such events during the entire satellite altimetric time series (Dencausse et al., submitted manuscript, 2009).

[56] From the altimetry time series, especially since the MADT product has been provided by CLS-AVISO [*Ducet et al.*, 2000; *Rio and Hernandez*, 2004], smaller mesoscale structures, and in particular cyclonic eddies, clearly appear [e.g., *Chelton et al.*, 2007]. We observe such structures at every GH hydrographic cruise. Cyclonic eddies and smaller anticylonic structures, that develop poleward, are starting to be tracked through different methods in a more quantitative way. *Sokolov and Rintoul* [2009b] found that cyclones are more numerous than anticyclones, and *Roullet and Klein* [2009], in a very high resolution numerical study of the ACC, found the same. The specific tracking of the cyclones has been initiated and finalized around the southern African slope [*Rubio et al.*, 2009], which also shows a slight majority of cyclonic structures (that are ejected from the continental slope) over anticyclonic eddies in the Cape Basin. This type of analyses (in the form of regional modeling and altimetry data analysis) should be extended to the ACC sector of the GH region to quantitatively evaluate the mesoscale characteristics and associated transport of these features.

[57] The propagation of Agulhas Rings into the northern domains of the ACC largely governs the anomalous behavior of the SAZ. These features are not consistently present in the region but on average they cross the GH line, south of the STF, 2.7 occasions per year. It is clear that the majority of the Agulhas Rings move out of the ACC region within a few months. However, a portion of their temperature, salinity and other property signals are likely to remain in the ACC, thereby providing an apparent mechanism for tropical-extratropical exchange. Furthermore, this study identifies an extremely anomalous episode of heat and salt content in the SAZ. The exploitation of the GEM allows us to better realize the impact these events have on the region by quantifying the subsurface temperature and salinity characteristics.

[58] Key topographic obstructions, namely the Mid-Ocean Ridge, Agulhas Ridge and Meteor Rise, play a fundamental role in determining the behavior of the fronts at the GH line. The SAF experiences large-scale meandering as the jet is forced northward by the Meteor Rise and generally inhibits the genesis of mesoscale eddies at the GH line. The opposite is true for the APF where, downstream of the Mid-Ocean Ridge, the input of relative vorticity is likely dissipated through nonlinear processes such as eddy action [*Hughes*, 1995]. This seems to be the obvious heat and salt content variability signal found at the APF and may therefore, be a key region in the formation of warm and cold eddies in the ACC.

[59] The time series of HCA and SCA within each front and frontal zone reveals the profound contribution the SAZ has to the total variability found in the ACC in the GH region (HC > 50%, SC > 60%). The proportion of variance introduced by the seasonal cycle was also calculated for each frontal zone. The results indicate that the seasonal cycle contributes a considerably greater portion of the total variance further to the south (~20% of variance explained at the SBdy) compared with the SAZ (~10%). This is likely caused by the higher amplitude of the seasonal cycle in the higher latitudes but also reiterates that the variability in the Subantarctic regions may be driven more extensively by communications with the subtropical oceanic domains and, in more general, by the highly nonlinear character of the flow. Both satellite altimetry and high-resolution modeling

studies have uncovered that fine-scale dynamics (mesoscale and submesoscale) play a major role in the Southern Ocean dynamics [*Hogg and Blundell*, 2006; *Chelton et al.*, 2007; *Thompson*, 2009; *Roullet and Klein*, 2009]. The connection with atmospheric forcing and the large-scale dynamics is therefore not as direct and linear as it was thought to be in previous studies [*Thompson and Solomon*, 2002; *Meredith et al.*, 2004; *Cai et al.*, 2003] and a dedicated study is needed to better understand this relationship.

[60] Last, the use of wavelet analysis on the time series component of this paper shows that longer (>1 year) temporal modes of variability are present at the SAZ, APF and APZ. A short comparison with the two most well-known modes of variability in the Southern Ocean indicates that there may be some connection between the long-term variability found in the APF region and with the SAM index, while the SOI appears to be well correlated with the extreme southern parts of the ACC. A detailed comparison with surface wind speed data for the region may possibly yield some interesting results, but does not fit into the scope of the study presented here.

[61] The exploitation of the proxy methods presented here are useful at improving our understanding of the subsurface properties that previously would have only been revealed by in situ sampling of the water column. However, we have to remain cautious in determining the scale of variability in the system using these techniques. The GEM is dependent on the height information at the sea surface to infer subsurface thermohaline information. As dynamic height is representative of the density signal throughout the water column, the GEM may not be able to precisely isolate variations in the heat and salt content within specific water masses and its strength is best suited at determining integrated property changes throughout the upper 2500 dbar of the water column. Additionally, at this stage we are unable to determine from what sources an increasing steric height signal may come from. This may be due to changes in the oceans heat content leading to thermal expansion of seawater or from mass input originating from melting continental ice [*von Schuckmann et al.*, 2009]. Moreover, it has recently been shown that mass input has a greater effect on steric height changes than initially thought [*Cazenave et al.*, 2008]. Nevertheless, the use of data derived from proxy methods provides an important tool to study the variability and dynamics of the ACC system on a continuous basis and at an improved spatial resolution. These techniques justify added effort to refine them and to employ them to answer key scientific questions in Southern Ocean oceanography. These include better quantifying the meridional exchanges and fluxes of heat and freshwater over the entire circumpolar path of the ACC.

[62] **Acknowledgments.** This research forms part of the first author's Ph.D., completed at the University of Cape Town, and funded by the NRF and SANAP. This work is part of the international CLIVAR GoodHope project. S. Speich has been supported by the University of Brest, IRD, and the National French Research Programme (LEFE). Thanks go to I. J. Ansorge and J. R. E. Lutjeharms for helpful comment and guidance during this research. S. Swart thanks A. Naveira-Garabato and W. P. M. de Ruijter for a stay at the National Oceanography Centre, Southampton, United Kingdom, and IMAU, Universiteit van Utrecht, Netherlands, respectively. The wavelet analysis MatLab tools were obtained from *Torrence and Compo* [1998] and adapted by B. Backeberg. The monthly time series of the SAM and SOI indexes were obtained from KNMI climate explorer website (http://climexp.knmi.nl). Thanks are extended to R. Blamey and N. Hart for helpful comments during the writing of this manuscript. The authors would like to thank two anonymous reviewers for their time in reviewing this paper.

## References

Ansorge, I. J., S. Speich, J. R. E. Lutjeharms, G. J. Goni, C. J. Rautenbach, W. Froneman, M. Rouault, and S. Garzoli (2004), Monitoring the oceanic flow between Africa and Antarctica, *S. Afr. J. Sci.*, *101*, 29–35.

Ansorge, I. J., J. R. E. Lutjeharms, N. C. Swart, and J. V. Durgadoo (2006), Observational evidence for a cross frontal heat pump in the Southern Ocean, *Geophys. Res. Lett.*, *33*, L19601, doi:10.1029/2006GL026174.

Belkin, I. M., and A. L. Gordon (1996), Southern Ocean fronts from the Greenwich meridian to Tasmania, *J. Geophys. Res.*, *101*, 3675–3696, doi:10.1029/95JC02750.

Boebel, O., J. R. E. Lutjeharms, C. Schmid, W. Zenk, T. Rossby, and C. Barron (2003), The Cape Cauldron: A regime of turbulent inter-ocean exchange, *Deep Sea Res.*, *50*, 57–86, doi:10.1016/S0967-0645(02)00379-X.

Bryden, H. L., L. M. Beal, and L. M. Duncan (2005), Structure and transport of the Agulhas Current and its temporal variability, *J. Oceanogr.*, *61*(3), 479–492, doi:10.1007/s10872-005-0057-8.

Cai, W., P. H. Whetton, and D. J. Karoly (2003), The response of the Antarctic Oscillation to increasing and stabilized atmospheric $CO_2$, *J. Clim.*, *16*, 1525–1538.

Cazenave, A., K. Dominh, S. Guinehut, E. Berthier, W. Llovel, G. Ramillien, M. Ablain, and G. Larnicol (2008), Sea level budget over 2003–2008: A reevaluation from GRACE space gravimetry, satellite altimetry and Argo, *Global Planet. Change*, *65*, 83–88, doi:10.1016/j.gloplacha.2008.10.004.

Chelton, D. B., M. G. Schlax, D. L. Witter, and J. G. Richman (1990), Geosat altimeter observations of the surface circulation of the Southern Ocean, *J. Geophys. Res.*, *95*, 17,877–17,903, doi:10.1029/JC095iC10p17877.

Chelton, D. B., M. G. Schlax, R. M. Samelson, and R. A. de Szoeke (2007), Global observations of large oceanic eddies, *Geophys. Res. Lett.*, *34*, L15606, doi:10.1029/2007GL030812.

Daniault, N., and Y. Menard (1985), Eddy kinetic energy distribution in the Southern Ocean from altimetry and FGGE drifting buoys, *J. Geophys. Res.*, *90*, 11,877–11,889, doi:10.1029/JC090iC06p11877.

Daubechies, I. (1992), *Ten Lectures on Wavelets*, 357 pp., Soc. for Ind. and Appl. Math., Philadelphia, Pa.

Deacon, G. E. R. (1933), A general account of the hydrology of South Atlantic Ocean, *Discovery Rep.*, *7*, 171–238.

de Ruijter, W. P. M., A. Biastoch, S. S. Drijfhout, J. R. E. Lutjeharms, R. P. Matano, T. Pichevin, P. J. van Leeuwen, and W. Weijer (1999), Indian-Atlantic interocean exchange: Dynamics, estimation and impact, *J. Geophys. Res.*, *104*, 20,885–20,910, doi:10.1029/1998JC900099.

Ducet, N., P. Y. Le Traon, and G. Reverdin (2000), Global high-resolution mapping of ocean circulation from TOPEX/Poseidon and ERS-1 and-2, *J. Geophys. Res.*, *105*, 19,477–19,498, doi:10.1029/2000JC900063.

Duncombe-Rae, C. M. (1991), Agulhas retroflection rings in the South Atlantic ocean: An overview, *S. Afr. J. Mar. Sci.*, *11*, 327–344.

Gladyshev, S., M. Arhan, A. Sokov, and S. Speich (2008), A hydrographic section from South Africa to the southern limit of the Antarctic Circumpolar Current at the Greenwich meridian, *Deep Sea Res. Part I*, *55*, 1284–1303, doi:10.1016/j.dsr.2008.05.009.

Gong, D., and S. Wang (1999), Definition of Antarctic Oscillation Index, *Geophys. Res. Lett.*, *26*, 459–462, doi:10.1029/1999GL900003.

Gordon, A. L. (1985), Indian-Atlantic transfer of thermocline water at the Agulhas Retroflection, *Science*, *227*, 1030–1033, doi:10.1126/science.227.4690.1030.

Gouretski, V. V., and A. I. Danilov (1994), Characteristics of warm rings in the African sector of the Antarctic Circumpolar Current, *Deep Sea Res. Part I*, *41*, 1131–1157, doi:10.1016/0967-0637(94)90037-X.

Hogg, A. M., and J. R. Blundell (2006), Interdecadal variability of the Southern Ocean, *J. Phys. Oceanogr.*, *36*, 1626–1645, doi:10.1175/JPO2934.1.

Hughes, C. W. (1995), Rossby waves in the Southern Ocean: A comparison of TOPEX/POSEIDON altimetry with model predictions, *J. Geophys. Res.*, *100*, 15,933–15,950, doi:10.1029/95JC01380.

Hughes, C. W. (1996), The Antarctic Circumpolar Current as a waveguide for Rossby waves, *J. Phys. Oceanogr.*, *26*, 1375–1387, doi:10.1175/1520-0485(1996)026<1375:TACCAA>2.0.CO;2.

Hughes, C. W., and E. R. Ash (2001), Eddy forcing of the mean flow in the Southern Ocean, *J. Geophys. Res.*, *106*(C2), 2713–2722.

Jones, J. M., R. L. Fogt, M. Widmann, and G. Marshall (2009), Historical SAM variability. Part I: Century-length seasonal reconstructions, *J. Clim.*, *22*, 5319–5345.

Joyce, T. M., W. Zenk, and J. M. Toole (1978), The anatomy of the Antarctic Polar Front in the Drake Passage, *J. Geophys. Res.*, *83*, 6093–6113, doi:10.1029/JC083iC12p06093.

Karoly, D. J. (1989), Southern Hemisphere circulation features associated with El Niño-Southern Oscillation events, *J. Clim.*, *2*, 1239–1252, doi:10.1175/1520-0442(1989)002<1239:SHCFAW>2.0.CO;2.

Koshlyakov, M. N., Y. M. Grachev, T. G. Sazhina, and M. I. Yaremchuk (1985), A cyclonic eddy in the Antarctic Circumpolar Current and heat transport across the Antarctic Front, *Oceanology Engl. Transl.*, *25*, 685–691.

Lau, K. M., and H. Weng (1995), Climate signal detection using wavelet transform: How to make a time series sing, *Bull. Am. Meteorol. Soc.*, *76*(12), 2391–2402, doi:10.1175/1520-0477(1995)076<2391:CSDUWT>2.0.CO;2.

Le Traon, P., P. F. Nadal, and N. Ducet (1998), An improved mapping method of multisatellite altimeter data, *J. Atmos. Oceanic Technol.*, *15*, 522–534, doi:10.1175/1520-0426(1998)015<0522:AIMMOM>2.0.CO;2.

Lutjeharms, J. R. E. (1988), Meridional heat transport across the Sub-Tropical Convergence by a warm eddy, *Nature*, *331*, 251–253, doi:10.1038/331251a0.

Lutjeharms, J. R. E. (1996), The exchange of water between the South Indian and South Atlantic oceans, in *The South Atlantic: Present and Past Circulation*, edited by G. Wefer et al., pp. 125–162, Springer, Heidelberg, Germany.

Lutjeharms, J. R. E. (2006), *The Agulhas Current*, 329 pp., Springer, Heidelberg, Germany.

Lutjeharms, J. R. E., and A. L. Gordon (1987), Shedding of an Agulhas Ring observed at sea, *Nature*, *325*, 138–140, doi:10.1038/325138a0.

Lutjeharms, J. R. E., and H. R. Valentine (1984), Southern Ocean thermal fronts south of Africa, *Deep Sea Res.*, *31*, 1461–1475, doi:10.1016/0198-0149(84)90082-7.

Lutjeharms, J. R. E., and H. R. Valentine (1988), Eddies at the Sub-Tropical Convergence south of Africa, *J. Phys. Oceanogr.*, *18*, 761–774, doi:10.1175/1520-0485(1988)018<0761:EATSCS>2.0.CO;2.

Mackintosh, N. A. (1946), The Antarctic Convergence and the distribution of surface temperatures in Antarctic waters, *Discovery Rep.*, *23*, 177–212.

Marshall, G. J. (2003), Trends in the Southern Annular Mode from observations and reanalysis, *J. Clim.*, *16*, 4134–4143, doi:10.1175/1520-0442(2003)016<4134:TITSAM>2.0.CO;2.

Melice, J. L., A. Coron, and A. Berger (2001), Amplitude and frequency modulations of the Earth's obliquity for the last million years, *J. Clim.*, *14*, 1043–1054, doi:10.1175/1520-0442(2001)014<1043:AAFMOT>2.0.CO;2.

Meredith, M. P., and A. M. Hogg (2006), Circumpolar response of Southern Ocean eddy activity to a change in the Southern Annular Mode, *Geophys. Res. Lett.*, *33*, L16608, doi:10.1029/2006GL026499.

Meredith, M. P., P. L. Woodworth, C. W. Hughes, and V. Stepanov (2004), Changes in the ocean transport through Drake Passage during the 1980s and 1990s, forced by changes in the Southern Annular Mode, *Geophys. Res. Lett.*, *31*, L21305, doi:10.1029/2004GL021169.

Mo, K. (2000), Relationships between low-frequency variability in the Southern Hemisphere and sea surface temperature anomalies, *J. Clim.*, *13*, 3599–3610, doi:10.1175/1520-0442(2000)013<3599:RBLFVI>2.0.CO;2.

Mo, K., and G. White (1985), Teleconnections in the Southern Hemisphere, *Mon. Weather Rev.*, *113*, 22–37, doi:10.1175/1520-0493(1985)113<0022:TITSH>2.0.CO;2.

Moore, J. K., M. R. Abbott, and J. G. Richman (1997), Variability in the location of the Antarctic Polar Front (90–20°W) from satellite sea surface temperature data, *J. Geophys. Res.*, *102*, 27,825–27,833, doi:10.1029/97JC01705.

Moore, J. K., M. R. Abbot, and J. G. Richman (1999), Location and dynamics of the Antarctic Polar Front from satellite sea surface temperature data, *J. Geophys. Res.*, *104*(C2), 3059–3073.

Morrow, R., R. Coleman, J. Bhurch, and D. Chelton (1994), Surface eddy momentum flux and velocity variances in the Southern Ocean from Geosat altimetry, *J. Phys. Oceanogr.*, *24*, 2050–2071, doi:10.1175/1520-0485(1994)024<2050:SEMFAV>2.0.CO;2.

Morrow, R., J.-R. Donguy, A. Chaigneau, and S. R. Rintoul (2004), Cold-core anomalies at the Subantarctic Front, south of Tasmania, *Deep Sea Res. Part I*, *51*, 1417–1440.

Nowlin, W. D., and J. M. Klinck (1986), The physics of the Antarctic Circumpolar Current, *Rev. Geophys. Space Phys.*, *24*, 469–491, doi:10.1029/RG024i003p00469.

Orsi, A. H., T. Whitworth, and W. D. Nowlin (1995), On the meridional extent and fronts of the Antarctic Circumpolar Current, *Deep Sea Res.*, *42*, 641–673, doi:10.1016/0967-0637(95)00021-W.

Patterson, S. (1985), Surface circulation and kinetic energy distribution in the Southern Hemisphere oceans from FGGE drifting buoys, *J. Phys. Oceanogr.*, *15*, 865–884, doi:10.1175/1520-0485(1985)015<0865:SCAKED>2.0.CO;2.

Philander, S. G. H. (1990), *El Niño, La Niña and the Southern Oscillation*, 289 pp., Academic, San Diego, Calif.

Phillips, H. E., and S. R. Rintoul (2000), Eddy variability and energetics from direct current measurements in the Antarctic Circumpolar Current south of Australia, *J. Phys. Oceanogr.*, *30*, 3050–3076, doi:10.1175/1520-0485(2000)030<3050:EVAEFD>2.0.CO;2.

Rasmusson, E. M., and T. Carpenter (1982), Variations in tropical sea surface temperature and surface wind fields associated with the Southern Oscillation/El Niño, *Mon. Weather Rev.*, *110*, 354–384, doi:10.1175/1520-0493(1982)110<0354:VITSST>2.0.CO;2.

Rauthe, M., A. Hense, and R. Morrow (2004), A model intercomparison study of climate change signals in extratropical circulation, *Int. J. Climatol.*, *24*, 643–662, doi:10.1002/joc.1025.

Richardson, P. L. (1983), Eddy kinetic energy in the North Atlantic from surface drifters, *J. Geophys. Res.*, *88*(C7), 4355–4367, doi:10.1029/JC088iC07p04355.

Rio, M. H., and F. Hernandez (2004), A mean dynamic topography computed over the world ocean from altimetry, in situ measurements, and a geoid model, *J. Geophys. Res.*, *109*, C12032, doi:10.1029/2003JC002226.

Roullet, G., and P. Klein (2009), Available potential energy diagnosis in a direct numerical simulation of rotating stratified turbulence, *J. Fluid Mech.*, *624*, 45–55, doi:10.1017/S0022112008004473.

Rubio, A., B. Blanke, S. Speich, N. Grima, and C. Roy (2009), Mesoscale eddy activity in the southern Benguela upwelling system from satellite altimetry and model data, *Prog. Oceanogr.*, *83*, 288–295, doi:10.1016/j.pocean.2009.07.029.

Sallee, J. B., K. Speer, and R. Morrow (2008), Southern Ocean fronts and their variability to climate modes, *J. Clim.*, *21*(12), 3020–3039, doi:10.1175/2007JCLI1702.1.

Schonten, M. V., W. P. M. de Ruijter, P. J. van Leeuwen, and J. R. E. Lutjeharms (2000), Translation, decay and splitting of Agulhas Rings in the south-eastern Atlantic Ocean, *J. Geophys. Res.*, *105*, 21,913–21,925, doi:10.1029/1999JC000046.

Sokolov, S., and S. R. Rintoul (2007a), Multiple jets of the Antarctic Circumpolar Current south of Australia, *J. Phys. Oceanogr.*, *37*, 1394–1412, doi:10.1175/JPO3111.1.

Sokolov, S., and S. R. Rintoul (2007b), On the relationship between fronts of the Antarctic Circumpolar Current and surface chlorophyll concentrations in the Southern Ocean, *J. Geophys. Res.*, *112*, C07030, doi:10.1029/2006JC004072.

Sokolov, S., and S. R. Rintoul (2009a), Circumpolar structure and distribution of the Antarctic Circumpolar Current fronts: 1. Mean circumpolar paths, *J. Geophys. Res.*, *114*, C11018, doi:10.1029/2008JC005108.

Sokolov, S., and S. R. Rintoul (2009b), Circumpolar structure and distribution of the Antarctic Circumpolar Current fronts: 2. Variability and relationship to sea surface height, *J. Geophys. Res.*, *114*, C11019, doi:10.1029/2008JC005248.

Speich, S., and M. Arhan (2007), GOODHOPE/Southern Ocean: A study and monitoring of the Indo-Atlantic connections, *Mercator Newslett.*, *27*, 29–41.

Stammer, D. (1998), On eddy characteristics, eddy transports, and mean flow properties, *J. Phys. Oceanogr.*, *28*, 727–739, doi:10.1175/1520-0485(1998)028<0727:OECETA>2.0.CO;2.

Sun, C., and D. R. Watts (2001), A circumpolar gravest empirical mode for the Southern Ocean hydrography, *J. Geophys. Res.*, *106*, 2833–2855, doi:10.1029/2000JC900112.

Swart, S., S. Speich, I. J. Ansorge, G. J. Goni, S. Gladyshev, and J. R. E. Lutjeharms (2008), Transport and variability of the Antarctic Circumpolar Current south of Africa, *J. Geophys. Res.*, *113*, C09014, doi:10.1029/2007JC004223.

Swart, S., S. Speich, I. J. Ansorge, and J. R. E. Lutjeharms (2010), An altimetry-based gravest empirical mode south of Africa: 1. Development and validation, *J. Geophys. Res.*, doi:10.1029/2009JC005299, in press.

Thompson, A. F. (2009), Jet formation and evolution in baroclinic turbulence with simple topography, *J. Phys. Oceanogr.*, doi:10.1175/2009JPO4218.1, in press.

Thompson, D. W. J., and S. Solomon (2002), Interpretation of recent Southern Hemisphere climate change, *Science*, *296*, 895–899, doi:10.1126/science.1069270.

Torrence, C., and G. P. Compo (1998), A practical guide to wavelet analysis, *Bull. Am. Meteorol. Soc.*, *79*, 61–78, doi:10.1175/1520-0477(1998)079<0061:APGTWA>2.0.CO;2.

Troup, A. J. (1965), The Southern Oscillation, *Q. J. R. Meteorol. Soc.*, *91*, 490–506.

von Schuckmann, K., F. Gaillard, and P.-Y. Le Traon (2009), Global hydrographic variability patterns during 2003–2007, *J. Geophys. Res.*, *114*, C09007, doi:10.1029/2008JC005237.

Wunsch, C., and D. Stammer (1995), The global frequency-wavenumber spectrum of oceanic variability estimated from TOPEX/POSEIDON altimetric measurements, *J. Geophys. Res.*, *100*(C12), 24,895–24,910, doi:10.1029/95JC01783.

Yuan, X. (2004), ENSO-related impacts on Antarctic sea ice: A synthesis of phenomenon and mechanisms, *Antarct. Sci.*, *16*(4), 415–425, doi:10.1017/S0954102004002238.

S. Speich, Laboratoire de Physique des Océans, UMR 6523, Université de Bretagne Occidentale, CNRS, IFREMER, 6 Ave. Le Gorgeu, F-29238 Brest, France.

S. Swart, Department of Oceanography, University of Cape Town, Private Bag, Rondebosch 7701, South Africa. (sebastiaan.swart@uct.ac.za)